Eddy–Mean Flow Interaction in Zonal Oceanic Jet Flow along Zonal Ridge Topography

DONNA L. WITTER* AND DUDLEY B. CHELTON

College of Oceanic and Atmospheric Sciences, Oregon State University, Corvallis, Oregon

(Manuscript received 17 December 1996, in final form 19 December 1997)

ABSTRACT

Motivated by satellite altimeter observations of enhanced sea level variability near steep topographic slopes in the Southern Ocean, effects of topography on the spatial distribution of mesoscale eddies and on eddy–mean flow interaction are investigated using a two-layer, wind-forced, quasigeostrophic channel model. The principal topography, a zonal ridge with a zonal modulation of ridge height and width, is an idealized version of a segment of the Southeast Indian Ridge along the path of the Antarctic Circumpolar Current. Geosat altimeter observations in this region suggest that spatial variations of eddy energy are related to alongstream modulations of ridge morphology.

The time-mean flow and distribution of time-dependent eddies in the model are sensitive to relatively subtle alongstream variations of topography. Topographic steering leads to alongstream variations of time-mean baroclinic and barotropic shear and to alongstream variations in the meridional position of the jet relative to the crest of the zonal ridge. Linear stability analysis demonstrates that zonal variations of flow stability are strongly coupled to the topography. Unstable mode growth rates are largest where topographic steering forces the jet into regions of reduced ambient potential vorticity gradient. Growth rates are lower where topography steers the jet into regions of higher ambient potential vorticity gradient. As a result, the largest eddy energies occur downstream of zonal modulations of ridge height or width. Unlike flows over flat-bottom topography, the zonal distribution of unstable mode growth rate is negatively correlated with velocity shear. Analysis of area-averaged mean-to-eddy energy conversions shows that zonal modulations of topography modify the regime of flow instability. Baroclinic instability and recycling of eddy energy in the upper part of the water column occur in cases with zonally uniform topography. Mixed baroclinic–barotropic instability and strong downward transfers of eddy energy occur in cases with zonal modulations of topography. Local vorticity analyses demonstrate that alongstream variations of topography produce strong zonal modulations of flow dynamics. Zonal variations of topography shift the region of eddy-influenced dynamics within the model domain and modify the relative contributions of the mean and eddy field to the time-mean vorticity balance. When interpreted in the context of Southern Ocean dynamics, these results suggest that eddy-active regions near steep topographic slopes may contribute disproportionately to the dynamics of the Antarctic Circumpolar Current.

1. Introduction

The strong visual correlation between transient eddy energy and topography in the Southern Ocean suggests that topography may control the stability of some segments of the Antarctic Circumpolar Current (ACC). As a result, topography may contribute significantly to local and regional dynamics, both through its effect on the time-mean flow and its effect on eddy-mean flow interactions. The probable influence of topography on local Southern Ocean (SO) dynamics is clearly demonstrated by satellite altimeter observations (Sandwell and Zhang 1989; Chelton et al. 1990) and drifter observations (Patterson 1985), which show that high eddy energy is preferentially found near strong time-mean flows and steep topographic gradients; lower eddy energy occurs in regions of weaker mean flows or weak topographic slopes. Arriving at a more general understanding of the stability of the ACC as a whole and explaining the details of the topographic contribution to regional and large-scale ACC dynamics is, however, challenging; resolving both the time-mean and transient components of SO flow is difficult from the existing observational database. In this study, we use a process-modeling approach to investigate local and large-scale interactions between topography and idealized oceanic jet flows.

Observations from the few regions of the SO that have been sampled at high spatial and temporal resolution suggest that the development of mesoscale eddies can be attributed to the growth of instabilities along ACC jets. Examples of this include the Drake Passage

* Current affiliation: Lamont-Doherty Earth Observatory of Columbia University, Palisades, New York.

Corresponding author address: Dr. Donna L. Witter, Lamont-Doherty Earth Observatory of Columbia University, Rt. 9W, Palisades, NY 10964.
E-mail: dwitter@ldeo.columbia.edu

region, where eddy properties conform with those expected from baroclinic instability (Bryden 1979; Peterson et al. 1982; Inoue 1985), and the region southeast of New Zealand, where current meter velocities are consistent with a regime of barotropic instability (Bryden and Heath 1985). Observational studies also suggest that eddy–mean flow interactions may be important to SO dynamics. For example, vertical transfers of momentum by baroclinically unstable eddies may balance the input of eastward momentum by the wind (Johnson and Bryden 1989); horizontal fluxes of momentum by transient eddies may maintain the near-surface time-mean flow along some segments of the ACC (Morrow et al. 1994). Transient eddies may also transport significant quantities of heat across the Antarctic Polar Front (deSzoeke and Levine 1981). The relation between eddy energy and topography evident in the altimeter and drifter observations suggests that the magnitude and sign of each of these exchanges may be locally influenced by topography.

A number of recent model analyses have addressed the issues of local variations of SO dynamics and the effects of topography on the large-scale balance of the ACC. Analytical and numerical models have elucidated the role of topography on the zonal and alongstream momentum balances of the SO (Munk and Palmén 1951; Gill 1968; Gill and Bryan 1971; Johnson and Hill 1975; Johnson and Bryden 1989; Wolff et al. 1991; Killworth and Nanneh 1994; Ivchenko et al. 1996). Models have also proven useful for evaluating effects of topographic steering on the path and local dynamics of the ACC (Marshall 1995b; Gille 1995; Hughes and Killworth 1995; Gille 1997a,b). Work with near-eddy-resolving primitive equation simulations such as the Semtner and Chervin (SC) global ocean model (Semtner and Chervin 1988, 1992; Semtner 1995) and the Fine Resolution Antarctic Model (FRAM: Webb et al. 1991) supports the regional interpretation of SO dynamics suggested by satellite altimeter and drifter observations. For example, local momentum balances from the SC model indicate that the magnitudes of individual contributions to the balance vary along the path of the ACC (Gille 1995, 1997b). Analysis of the time-mean vorticity budget from the same model suggests that transient eddies contribute significantly to the maintenance of time-mean potential vorticity balance near major topographic features (Gille 1995, 1997a). A survey of the vertically integrated vorticity balance from FRAM suggests that the magnitudes of individual terms in the momentum balance vary along streamlines (Wells and deCuevas 1995). While the development of nearly eddy-resolving primitive equation models (e.g., SC and FRAM) has compensated, to a degree, for the relative sparseness of the in situ SO database, the computational resources required by these models hampers attempts at systematically investigating links among topography, mesoscale eddies, and the larger-scale SO flow. At present, studies of the sensitivity of eddy–mean flow interaction to topographic forcing are more feasible with simple models.

In this paper, we use a two-layer quasigeostrophic (QG) model to investigate relationships between transient eddies, the time-mean flow, and topography in a system with simple wind forcing and zonal geometry. A segment of the ACC south of Australia provides the framework for our experiments. In this region, variations of eddy energy correspond particularly well with alongstream variations of the underlying Southeast Indian Ridge (SEIR) topography (Fig. 1). The axis of the SEIR between 100° and 140°E is nearly zonal. Alongstream variations of ridge morphology are associated with the Australian–Antarctic Discordance (AAD), which represents a local minimum of ridge height and width at 50°S, 125°E (Hayes and Conolly 1972). Sea level variations mapped from the Geosat altimeter show low variability upstream of the AAD and several local maxima along the north flank of the ridge (Fig. 1). Beginning at the longitude of the AAD, a tongue of high variability extends downstream. Values of sea level variance in this tongue are 3–4 times larger than values over the abyssal plains to the north and south and 10 times larger than the background noise level. This local maximum of variability is also reproduced in potential vorticity estimates from hydrographic observations (Gille 1995).

Relations among topography, the structure of the time-mean flow, and the geographical distribution of time-dependent eddies are evaluated for three zonal ridge topographies. The principal topography is an idealized representation of the SEIR south of Australia. Two other zonal ridge topographies are considered for comparison. The numerical model and the idealized topographies are described in section 2. Model kinematics, including the structure of the time-mean flow and the spatial distribution of eddy kinetic energy, are evaluated in sections 3 and 4. The dynamical relationship between topography and the stability of the large-scale flow is assessed in section 5 based on linear stability analysis. Effects of zonal modulations of topography on the domain-averaged and regional dynamics are investigated in sections 6 and 7 using time-mean energy balances and time-mean vorticity budgets.

2. Numerical experiments

a. The numerical model

The numerical simulations were performed using a two-layer version of a QG channel model developed for process studies of ACC dynamics (McWilliams et al. 1978). This model applies to large-scale flows for which the Rossby number ($\mathrm{Ro} = U/f_0L$) is small and the aspect ratio (L/D) of horizontal to vertical motions is large. In this limit, the primitive equations reduce to the hydrostatic and geostrophic balances at leading order. At the next order, $O(\mathrm{Ro})$, effects of forcing, friction, inertia,

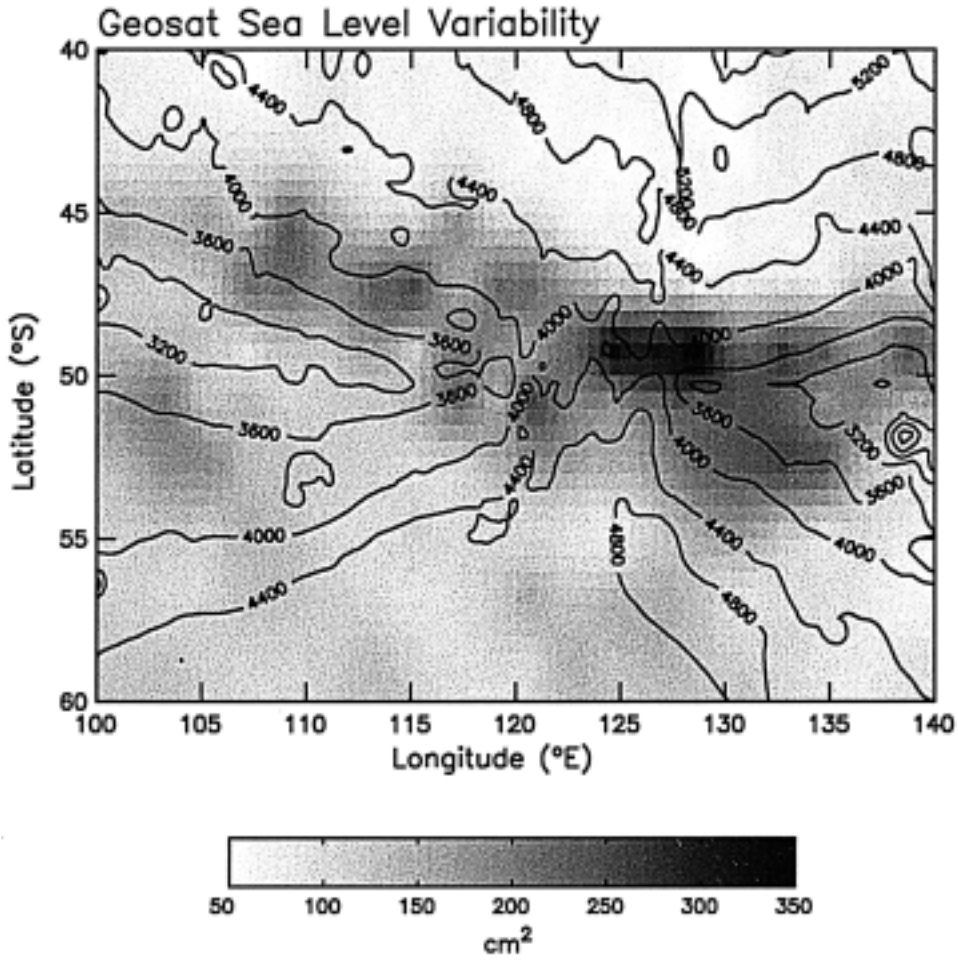

FIG. 1. Geosat sea level height variance (gray shading) and bathymetry (contours, ci = 400 m) near the Australian–Antarctic Discordance south of Australia.

and the planetary vorticity gradient appear in the momentum equations; topography modifies the bottom boundary condition through the continuity equation.

In each model layer, the O(Ro) momentum and continuity equations combine to form a vorticity equation:

$$\frac{\partial}{\partial t} Q_1 = J(Q_1, \psi_1) + \frac{\text{curl}_z \boldsymbol{\tau}}{\rho_0 H_1} - A_6 \nabla^6 \psi_n, \qquad (1a)$$

$$\frac{\partial}{\partial t} Q_2 = J(Q_2, \psi_2) - c_b \nabla^2 \psi_2 - A_6 \nabla^6 \psi_n, \qquad (1b)$$

where Q_n, the quasigeostrophic potential vorticity in layer n, is given by

$$Q_1 = \nabla^2 \psi_1 - \frac{f_0^2}{g' H_1}(\psi_1 - \psi_2) + f_0 + \beta y \qquad (1c)$$

$$Q_2 = \nabla^2 \psi_2 + \frac{f_0^2}{g' H_2}(\psi_1 - \psi_2) + f_0 + \beta y + \frac{f_0 h_b}{H_2} \qquad (1d)$$

for the surface and deep layers, respectively, and J is the horizontal Jacobian operator. The streamfunction in layer n, ψ_n, is related to u_n and v_n, the zonal and meridional geostrophic velocity components in layer n, by

$$u_n = -\frac{\partial \psi_n}{\partial y} \qquad v_n = +\frac{\partial \psi_n}{\partial x}. \qquad (2)$$

Forcing and friction in Eq. (1) are specified by the wind stress $\boldsymbol{\tau}$ and the bottom friction coefficient c_b. Biharmonic friction, with constant coefficient A_6 is used to account for effects of subgrid-scale dissipation (Holland 1978). Topography, h_b, directly affects the vorticity only in the deep layer. Communication between model layers is accomplished by vortex stretching associated with motion of the interface between homogeneous, immiscible layers of fluid with different densities.

Other model parameters include $g' = g(\rho_2 - \rho_1)/\rho_0$, the reduced gravity at the interface; ρ_1 and ρ_2, the densities of the surface and deep layers; ρ_0, a reference density; $f = f_0 + \beta y$, the β-plane approximation of the Coriolis parameter; and H_n is the undisturbed depth of layer n. Numerical values of these parameters (see Table 1) are chosen based on values used in previously

TABLE 1. Model parameters.

Channel length	L_x	4320 km
Channel width	L_y	1200 km
Grid spacing	Δs	20 km
Layer depths	H_1	1000 m
	H_2	4000 m
Reduced gravity	g'	0.02 m s^{-2}
Rossby radius	R_0	36.4 km
Time step	Δt	1.6 h
Sampling interval		5 days
Sampling period		7200 days
Coriolis parameters	f_0	-1.1×10^{-4} s^{-1}
	β	1.4×10^{-11} m^{-1} s^{-1}
Wind forcing	$\tau^{(x)}$	$\tau_0 \sin^2(\pi y/L_y)$
	τ_0	0.025 N m^{-2}
Bottom friction	c_b	1.0×10^{-7} s^{-1}
Biharmonic friction	A_6	1.0×10^{10} m^4 s^{-1}

published experiments (e.g., McWilliams et al. 1978; McWilliams and Chow 1981; Treguier and McWilliams 1990). As in these and other QG simulations of SO circulation (e.g., Wolff et al. 1991), the first baroclinic Rossby radius in the model is set to a value approximately 1.5–2 times larger than observed for computational efficiency. As a result of this artificially large stratification, communication between model layers is somewhat reduced in the numerical solutions (Marshall 1995a,b). Effects of topography on the upper layer flow and the quantity of eddy energy in the lower layer are therefore smaller in the model than in SO observations. Even with these simplifications, the QG model has several advantages in the context of the present investigation. Most notably, the QG model allows a process-oriented approach, where the relationship between eddy–mean flow interaction and topography is investigated through a series of sensitivity experiments. At the same time, QG dynamics are sufficiently complex to represent the baroclinic and barotropic instability processes believed to produce much of the eddy variability along the ACC (see Bryden 1983).

b. Topography and wind forcing

The series of experiments discussed below consists of three simulations that differ only in topographic configuration (Fig. 2). Flow over a zonally uniform ridge 400 m tall and 800 km wide (case 1) is compared with a simulation that includes a zonal modulation of ridge height (case 3) and with a simulation that includes a zonal modulation of ridge height and width (case 6). Of these, case 6 is the most similar to the topography near the AAD. These three cases represent a subset of a more extensive series of experiments (see Witter 1995). Note that a flat-bottom case, $h_b(x, y) = 0$, was also run for the parameters listed in Table 1. Because this geometry has been discussed extensively in the literature (McWilliams et al. 1978; McWilliams and Chow 1981; Treguier and McWilliams 1990; Wolff et al. 1991), results from this simulation are described only briefly.

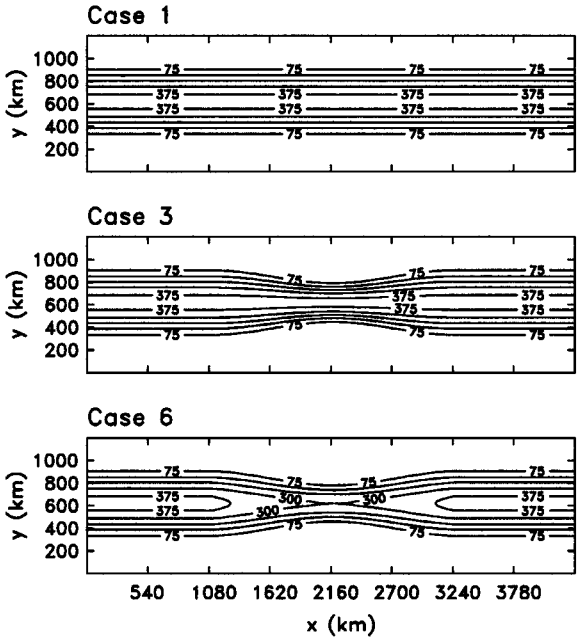

FIG. 2. Zonal ridge topography for cases 1, 3, and 6 (ci = 75 m).

Because the focus of this study is on the contribution of local variations of topography to local variations of flow properties, the functional form of the wind forcing is chosen for its simplicity. A steady, zonal wind jet with maximum stress at the center of the channel (y = 600 km) serves as the primary source of eastward momentum for the oceanic flow. This wind produces oceanic flow with both horizontal and vertical velocity shear. The maximum amplitude of the wind stress (τ_0) provides oceanic transport that agrees with observed ACC transports to within a factor of 2. The value of τ_0 required to maintain this level of transport is considerably smaller than wind stress values normally observed at high southern latitudes (see Table 1). This reduction is necessary because the major sink of wind-input momentum to the SO, namely, topographic form stress associated with steep meridional barriers to the ACC (Gille 1995, 1997b), is absent in case 1 and small relative to SO values in cases 3 and 6. Increasing or decreasing τ_0 by a factor of 2 does not alter the major conclusions of this paper (see Witter 1995).

In addition to the steady zonal wind forcing, a small amplitude wind perturbation is applied in case 1 during the first 200 days of the experiment to facilitate the transition from purely zonal flow to statistically steady turbulent flow. The structure of the time-mean flow and distribution of eddies during the statistically steady portion of the experiment are not sensitive to the detailed form of this perturbation. This perturbation is not necessary in cases 3 and 6 where zonal variations of topography induce a meridional velocity field.

c. Boundary conditions and sampling

The potential vorticity equations [Eq. (1)] are discretized on a 20-km grid, and derivatives are represented using centered differences. The model is then solved for the streamfunction in each layer subject to free slip and no normal flow conditions at the north and south boundaries of the domain and a cyclic condition at the east and west boundaries. Integral constraints on the mass and zonal momentum of each layer are specified to ensure that the problem is well posed (see McWilliams 1977). An additional boundary condition, $\nabla^4\psi_n = 0$, is applied along the north and south channel walls for mathematical consistency with the biharmonic friction operator.

For each choice of topography, the model is spun up from rest. The zonal transport, area-averaged kinetic energy of each layer, area-averaged potential energy at the interface, and spatial distribution of transient eddies are monitored during spinup. Based on these diagnostics, a 7200-day period of approximate statistical equilibrium is chosen for analysis. Diagnostics discussed in the following sections are computed from 1440 snapshots of the layered streamfunction field taken at 5-day intervals during the 7200-day sampling period for each experiment. The time-mean flow is defined as the arithmetic average of the 1440 instantaneous streamfunction samples. Deviations from this mean are defined as the eddy field. Although the flow is nonlinear, the Rossby number ($\nabla^2\psi_1/f$) remains small throughout layer 1 during the statistically steady phase of each simulation; the Rossby number is less than 0.3 at more than 90% of the layer 1 grid points and less than 0.15 at more than 70% of the layer 1 grid points. Rossby numbers are considerably smaller for the weaker flow of layer 2.

In the discussion below, the value of x corresponding to the point of minimum ridge height or width ($x = 2160$ km) is referred to below as x_{mid}; regions of the model domain at smaller and larger values of x are referred to as ''downstream'' and ''upstream,'' respectively. These directions generally correspond to the direction of the time-mean flow. The influence of the cyclic boundary condition on the flow near x_{mid} is small owing to the choice of domain size; sensitivity studies (see Witter 1995) demonstrated that the zonal dimension (L_x) of the model domain is large enough to allow the flow to evolve downstream of the variation of topography before encountering the cyclic condition at $x = 4320$ km. Because the channel includes cyclic geometry, the flow dynamics do not depend on the location of the zonal modulation of topography relative to the eastern end of the channel. The meridional dimension (L_y) of the domain is large enough to limit interaction between the jet flow of interest and the north and south channel walls (see Witter 1995).

3. Time-mean flow

For the large-scale oceanic flows of interest to this study, production of eddy energy occurs primarily through instabilities associated with vertical or horizontal shear. Shear instabilities have been discussed extensively in the atmospheric and oceanic literature (e.g., see Pedlosky 1987). Briefly, baroclinic instabilities convert available potential energy associated with mean vertical shear to eddy potential energy; barotropic instabilities convert kinetic energy associated with mean horizontal shear to eddy kinetic energy. Relations between the mean and eddy fields generally become more complex as the geometry of the problem becomes more complicated or as the flow becomes more nonlinear (see Pedlosky 1987). In all cases, properties of the mean flow are fundamental to the kinematics and dynamics of eddies.

For the three topographies considered here, the time-mean streamfunction consists of a jet in both model layers (Fig. 3). The layer 1 jet is directly forced by the input of eastward momentum by the wind. The layer 2 jet acquires momentum from the meridional pressure gradient associated with the large-scale interface tilt and from downward transfers of eastward momentum by baroclinic eddies. Topography directly affects the vorticity balance of the deep flow; the influence of topography is transmitted to the surface layer via vertical stretching at the interface.

In case 1, the model geometry cannot support a time-mean meridional velocity field; thus the time-mean flow is zonal. As shown in Fig. 3, the axis of the surface jet lies to the north of the line of zero wind stress curl; the deep jet is narrower and flows along the south flank of the ridge. The meridional offset between the surface and deep jets is not predicted by linear models of flow along zonal ridges (McCartney 1976). This offset is produced during the approach to a statistically steady state by interactions among time-dependent eddies, the topography, and the time-mean flow. During the initial stage of model spinup (see Witter 1995), the surface and deep jets are laminar and centered at the line of zero wind stress curl ($y = 600$ km). As eastward momentum is added to the flow by the wind, vertical shear increases, leading to the development of baroclinic instabilities. Meridional momentum fluxes associated with the nonlinear development of these unstable waves act as a feedback on the dynamics of the larger-scale flow. Eddies transfer momentum from the southern to the northern part of the domain in layer 1, displacing the jet toward the north flank of the ridge. A transfer in the opposite sense displaces the deep jet toward the south flank of the ridge. This response to topography can be compared with the time-mean flow obtained for two-layer QG flow over a flat bottom (see McWilliams et al. 1978, their Fig. 3). In the latter case, both the surface and deep time-mean jets are centered at the zero of wind stress curl. Because zonal ridge topography induces a meridional offset between the surface and deep time-mean jets, baroclinic shear is larger in the case with zonal ridge topography than for the flat-bottom case. For simulations with parameters given in Table 1, the

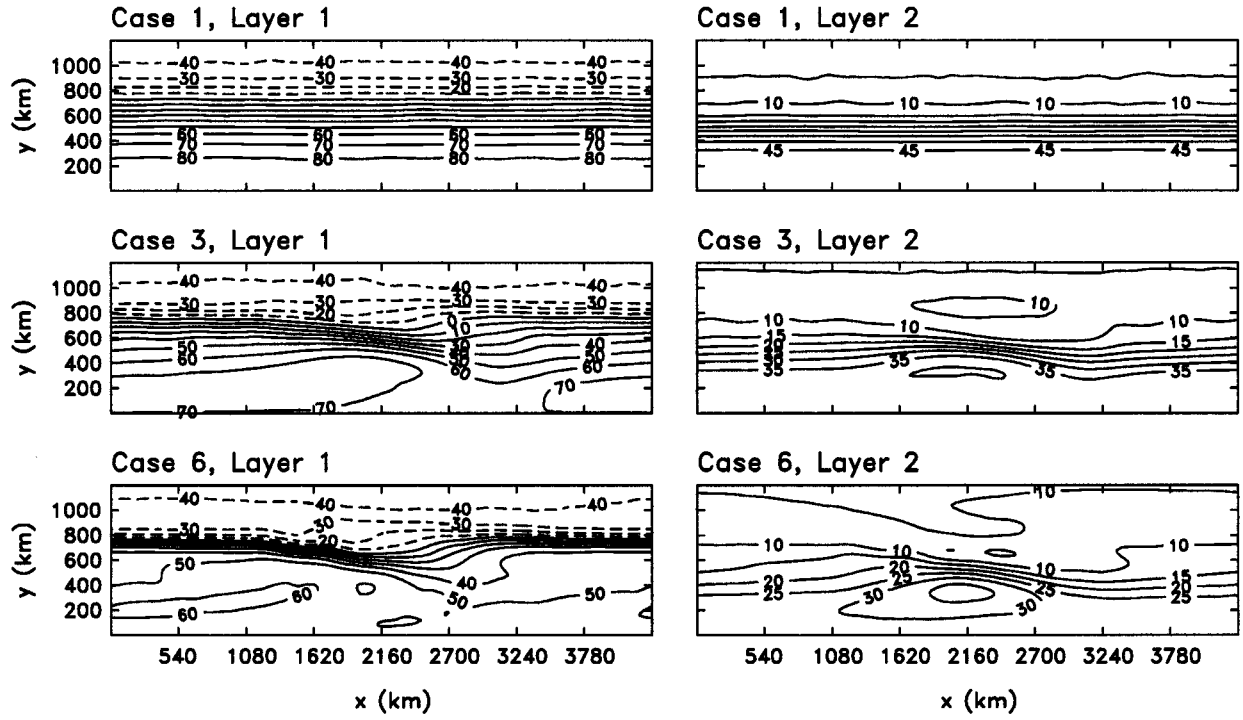

FIG. 3. Time-mean streamfunction for cases 1, 3, and 6. Layer 1, left panels (ci = 10 000 m^2 s^{-1}). Layer 2, right panels (ci = 5000 m^2 s^{-1}).

maximum baroclinic shear is 15% larger in case 1 than in the corresponding flat-bottom experiment.

The introduction of a zonal modulation of topography has two notable effects on the time-mean flow (see Fig. 3). The primary effect of topography is to steer the time-mean jet in a manner consistent with the contours of $f/\overline{h}_n$, where $\overline{h}_n$ is the time-mean thickness of layer n. A comparison of time-mean streamlines and isolines of $f/\overline{h}_n$ (not shown) demonstrates that, to first order, the time-mean jet maintains a balance among planetary vorticity, topographic vorticity, and stretching vorticity in layer 2 and between planetary vorticity and stretching vorticity in layer 1. This correspondence is particularly good in regions upstream and downstream of x_{mid} where the equilibrium positions of the surface and deep jets coincide with strong meridional gradients of $f/\overline{h}_n$. In layer 1, the maximum gradient of $f/\overline{h}$ occurs along the north flank of the ridge where the interface slope acts in the same sense as the planetary vorticity gradient. In layer 2, the position of the time-mean jet coincides with the large $f/\overline{h}$ gradient along the south flank of the ridge. In both cases, deviations from a linear relation between the time-mean streamfunction and $f/\overline{h}_n$ are significant only near x_{mid} where eddies contribute significantly to the regional dynamics (also see §7). One consequence of this topographic steering is that horizontal and vertical shear vary along the jet. Vertical shear, which is important for baroclinic instability, is smallest near x_{mid} where the time-mean deep jet attains it peak velocity and the meridional offset between the time-mean surface and deep jets reaches its minimum.

A secondary effect of topography on the time-mean flow occurs as a result of eddy–mean flow interaction. In cases 3 and 6, topographic steering stabilizes the time-mean jet (relative to case 1). This allows larger time-mean horizontal shear, particularly in regions far from x_{mid}. The effect of zonal variations of topography on flow stability is one of the most interesting aspects of these experiments. It is discussed in detail in section 5.

Note that, even though the QG model is highly idealized, the time-mean flow for case 6 is in good qualitative agreement with observations of the large-scale flow near the AAD. Hydrographic and current meter measurements between 100° and 140°E show that the transport is largely confined to the subantarctic front jet, which follows the north flank of the ridge upstream of the AAD (Callahan 1971; Savchenko et al. 1978; Belkin and Gordon 1996). As the jet traverses the AAD, it is first deflected to the south near 125°E, and then to the north farther east (Gordon et al. 1978). The relatively good correspondence between these observations and the model suggests that the model reproduces the basic dynamics of this region of the SO with some fidelity.

4. Eddy variability

Regional variations of time-mean shear are expected from theory to produce spatial variations in the eddy

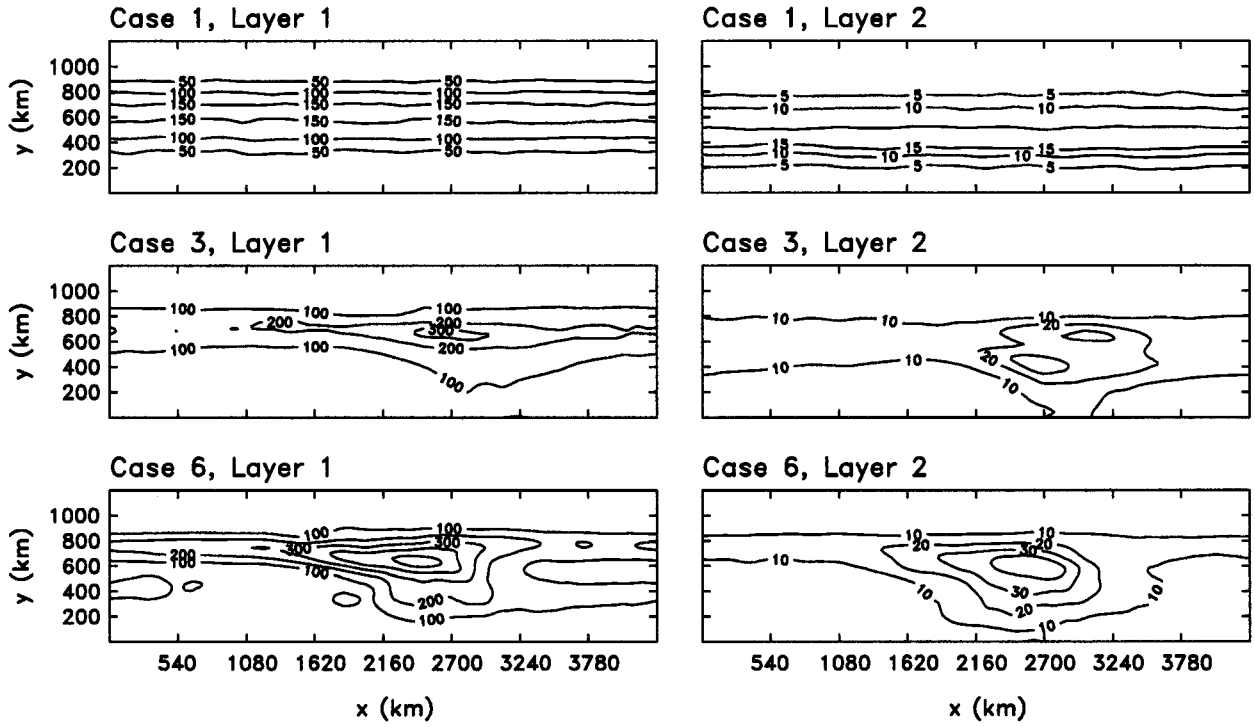

FIG. 4. Eddy kinetic energy per unit mass for cases 1, 3, and 6. Layer 1, left panels (ci = 50 cm^2 s^{-2} for case 1, ci = 100 cm^2 s^{-2} for cases 3 and 6). Layer 2, right panels (ci = 5 cm^2 s^{-2} for case 1, ci = 10 cm^2 s^{-2} for cases 3 and 6).

field (Pierrehumbert 1986; Samelson and Pedlosky 1990). The spatial distribution of time-dependent eddies was assessed in the model from the distribution of eddy kinetic energy per unit mass for each layer (K_n', $n = 1$, 2), where

$$K_n' = \frac{1}{2}(\overline{u_n'^2 + v_n'^2}),$$

and u_n' and v_n' are deviations from the time-mean geostrophic velocity components. A comparison of K_n' for the three experiments (Fig. 4) shows that the geographic distribution of eddy kinetic energy is strongly influenced by the structure of the topography.

In case 1, mechanisms that could support a zonal gradient of eddy kinetic energy are absent and the time-mean distribution of eddy energy is nearly zonally uniform (Fig. 4, top). Maxima in K' in the upper and lower layers are offset meridionally owing to the displacement of the surface and deep jets. These maxima result from the propagation of both stable and unstable waves along the jet. As waves propagate along the jet, the largest meanders detach, creating closed rings which are generally advected downstream by the large-scale flow. Narrower filaments, which separate from the crests and troughs of waves, stream to the north and south away from the core of the jet and generally move upstream before dissipating.

The zonal modulations of topography in cases 3 and 6 support an accumulation of eddy energy downstream of x_{mid} (Fig. 4). In case 3, the enhancement of K_1' along the core of the jet upstream and downstream of x_{mid} is produced by waves propagating along the jet, combined with intermittent eddy shedding and filament formation. Near x_{mid}, eddy shedding is particularly vigorous. Recirculation of mesoscale eddies in the region south of the jet contributes to the maximum of K_1' at $x = 2700$ km. In case 6, the spatial distribution of eddy energy is the result of several distinct eddy formation regimes. Upstream of x_{mid}, a combination of eastward wave propagation along the jet and detachment of filaments from wave crests and troughs produces a narrow region of high K_1'. However, unlike cases 1 and 3, the development of closed eddies is rare in this region; with few exceptions, ring formation occurs exclusively in the region downstream of x_{mid}. As meanders in the jet propagate downstream toward x_{mid}, their amplitudes increase. The largest wave troughs plunge to the south and detach from the jet as they reach x_{mid}. As in case 3, these closed eddies recirculate and dissipate in the region south and downstream of x_{mid}. Some of the closed eddies formed near x_{mid} follow a path along the south flank of the ridge before dissipating.

Even with the simplifications of QG dynamics, the distribution of K_1' in case 6 (Fig. 4, lower left) is strikingly similar to the observed distribution of sea level variability near the AAD (see Fig. 1). In both the model and observations, the region of highest eddy variability extends downstream of the minimum of ridge height

and width. The extension of the region of moderately high variability upstream of the AAD is captured, to a more limited degree, in the model.

5. Effects of topographic steering on local flow stability

a. Linear stability analysis

Spatial variations of the time-mean flow, such as those illustrated in Fig. 3, are important from the perspective of eddy–mean flow interaction because these variations may produce a zonal modulation of flow stability. In this section, estimates of flow stability are calculated based on linear stability analysis (LSA) of the model streamfunction fields. LSA provides the growth rate, phase speed, and structure of linearly unstable modes corresponding to any specified basic state streamfunction for any specified frictional parameterization, topography, stratification, and choice of β. The reader is referred to Haidvogel and Holland (1978) and Holland and Haidvogel (1980) for detailed descriptions of the LSA technique.

To determine whether the increase of eddy kinetic energy observed downstream of x_{mid} can be attributed to effects of topography on flow stability, the growth rate of the most unstable mode is calculated at ~270 km intervals along the channel. Both components of velocity (u and v), bottom friction, and the zonal and meridional variations of topography are included in the stability calculation. Results from analysis of the time-mean fields are then compared with LSA of a subset of instantaneous streamfunction fields. This consistency check provides some verification of the variations in stability evident from analysis of the time-mean flow.

Results from LSA of the time-mean flow demonstrate that the growth rate of the most unstable mode varies along the channel (Fig. 5a). Growth rates are largest in the region between $x = 1620$ km and $x = 2700$ km. Farther upstream and farther downstream, growth rates are two to five times smaller. This zonal variation of stability is consistent with the distributions of eddy energy shown in Fig. 4; in linearized analyses of local flow stability, maximum eddy amplitudes are located downstream of the maximum growth rate (Pierrehumbert 1986; Samelson and Pedlosky 1990). The zonal variation of stability is, however, somewhat at odds with alongstream variations of time-mean velocity shear (Fig. 5c). In particular, the flow is most unstable where baroclinic and barotropic shear is weakest; the flow is more stable where shear is stronger. Correlations between the maximum time-mean baroclinic shear and the linear growth rate are -0.38 and -0.28 in cases 3 and 6, respectively.

The negative correlation between mean shear and growth rate is not expected from analysis of unstable wave growth in purely baroclinic or purely barotropic flows over flat-bottom topography (see Pedlosky 1987).

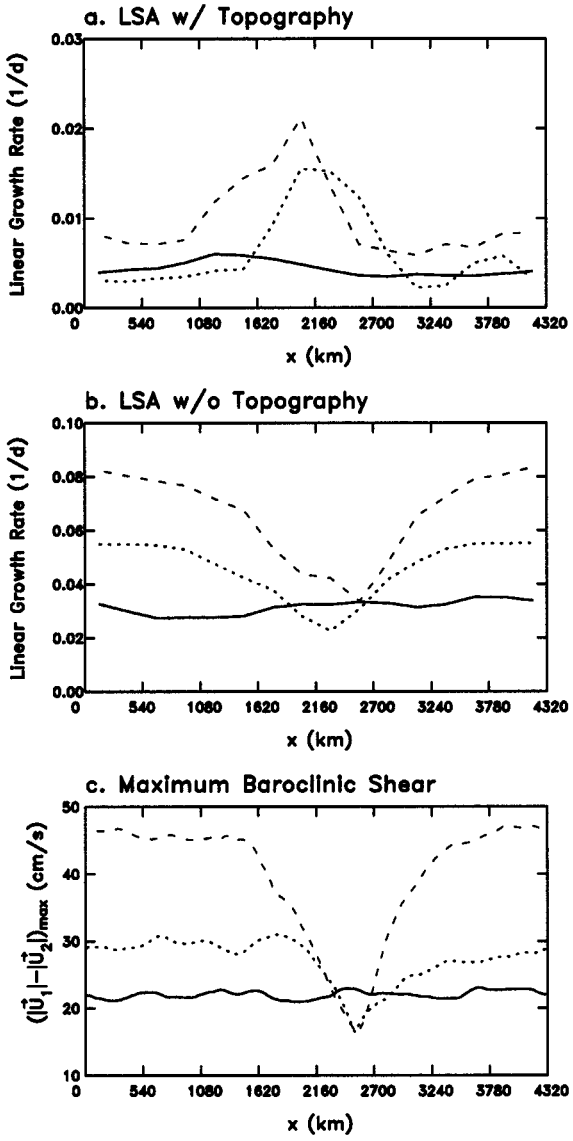

FIG. 5. Effect of the topographic contribution to the ambient potential vorticity gradient on the stability of the time-mean flow for cases 1 (solid), 3 (dotted), 5 and 6 (dashed). For each case, the growth rate of the most unstable mode is calculated from meridional sections through the time-mean flow at ≈270 km intervals using linear stability analysis. Growth rates calculated from adjacent sections are averaged to reduce point-to-point noise in the plot. The topography is included in the calculation shown in panel a and omitted in the calculation shown in panel b. The maximum time-mean baroclinic shear at each value of x is shown for comparison in panel c.

For these one-dimensional flows, growth rates increase with increasing shear. This negative correlation also cannot be explained by the model geometry; sensitivity studies (see Witter 1995) demonstrate that the spatial pattern of eddy energy, mean shear, and linear growth rate do not change if the channel length or width is increased. The apparent contradiction can, however, be explained by considering effects of topography on flow stability. Studies of the partial isomorphism between

topographic slopes and the planetary vorticity gradient β demonstrate that topography can influence flow stability through its effect on the ambient potential vorticity gradient[1] (Orlanski 1969; Samelson and Pedlosky 1990). Eastward flows are least stable over topographic slopes that counteract the planetary vorticity gradient (i.e., the south flank of the ridge in these Southern Hemisphere simulations).

To test whether the contribution of topography to the ambient potential vorticity gradient controls the stability of the time-mean flow, the growth rate of the most unstable mode is compared for calculations that include the topography and for those in which topography is omitted. In the latter calculations, the time-mean streamfunction from the numerical experiments including topography (Fig. 3) are used as the basic state for input to the LSA, but topographic terms are neglected in the LSA. The resulting alongstream variations of growth rate are plotted in Fig. 5b. Note that this calculation isolates the dynamical effect of topography on the stability of the flows in Fig. 3; it does not address the issue of how these particular time-mean flows are generated by the interaction of topography, the wind, and the internal model dynamics.

As expected, linear growth rates are controlled by the baroclinic shear if topography is neglected; alongstream correlations between growth rate and the maximum time-mean baroclinic shear are 0.47 and 0.96 in cases 3 and 6, respectively (Fig. 5b–c). In the far upstream and downstream regions, growth rates in Fig. 5b reflect that the baroclinic shear is high due to the meridional offset between the surface and deep jets and due to the strong zonal velocities in layer 1. Near x_{mid}, growth rates in Fig. 5b are smaller as a result of the smaller baroclinic and barotropic shear.

A comparison of Figs. 5a and 5b demonstrates that the simple relation between jet stability and time-mean shear is altered significantly by topography. The general reduction in growth rates from Fig. 5a to 5b indicates that the topography stabilizes the flow everywhere along the channel. This stabilizing influence is largest in regions where the maximum baroclinic shear occurs along the north flank of the ridge (i.e., far upstream and far downstream of x_{mid}). In these regions, the topographic slope increases the ambient potential vorticity gradient and exerts a strong stabilizing influence on the jet. In contrast, topographic steering near x_{mid} forces the time-mean jet over the ridge crest and to the south (see Fig. 3), where the smaller ambient potential vorticity gradient along the ridge crest allows larger growth rates. Thus, topographic steering, combined with the contribution of topographic slopes to the ambient potential vorticity gradient, inhibits wave growth upstream and downstream of x_{mid}. Near x_{mid}, topography steers the jet into a region of reduced meridional topographic slope where the stabilizing influence of the topographic slope is weaker. The resulting alongstream variation of stability allows the development of unstable eddies downstream of the zonal modulation of topography.

While the results from LSA of the time-mean fields are compelling, it is important to asses the degree to which stability of the total flow can be inferred from stability of the time-mean flow. This is accomplished by repeating the LSA using instantaneous streamfunction profiles as basic states. Twenty snapshots, at 360-day intervals, are analyzed for case 3 and for case 6. This computationally intensive procedure is not performed for the case of zonally uniform topography (case 1). Note that detailed, quantitative agreement is not expected for growth rates computed from the time mean and instantaneous profiles. The goal of this calculation is to ascertain whether the general relationship between topography and flow stability evident from analysis of the time-mean flow is consistent with relationships obtained from a less restrictive definition of the basic state.

For each snapshot, streamfunction profiles for input to the LSA are constructed by averaging over 360-km segments of the channel, separated by 540-km intervals (e.g., the profile corresponding to $x = 540$ km represents the x-averaged streamfunction between $x = 360$ km and $x = 720$ km). This smoothing reduces noise in the calculated growth rates by attenuating features with length scales comparable to or shorter than meanders propagating along the jet. Following the method used for the time-mean fields, topography was included in one set of LSA calculations and omitted in a second. To minimize noise from variability in the instantaneous growth rates, the sensitivity of zonal variations of flow stability to topography are inferred from the ''relative growth rate,'' defined as the growth rate of the most unstable mode computed with topography divided by that computed without topography. A relative growth rate equal to 1 indicates topography does not alter the stability of the jet; relative growth rates between 0 and 1 indicate that topography reduces growth of the most unstable mode. Results are plotted in Fig. 6 as a function of x, where the average relative growth rate at a given x is defined as the arithmetic average of the 20 estimates of relative growth rate at that x (one estimate from each snapshot). One standard deviation variations of the 20 estimates about their mean are indicated by the vertical bars.

It is clear from Fig. 6 that the stability of the instantaneous streamfunction fields are sensitive to alongstream variations of topography. Of particular interest is the general qualitative agreement between effects of topography on stability established from the time-mean analysis and that inferred from analysis of the instantaneous profiles. This agreement is particularly apparent in case 6; it holds to a more limited degree in case 3

[1] As used here, the ''ambient potential vorticity gradient'' refers to the sum of the planetary and topographic contributions to the potential vorticity gradient. Other contributions to the potential vorticity gradient depend on the flow field [see Eq. (1c–d)].

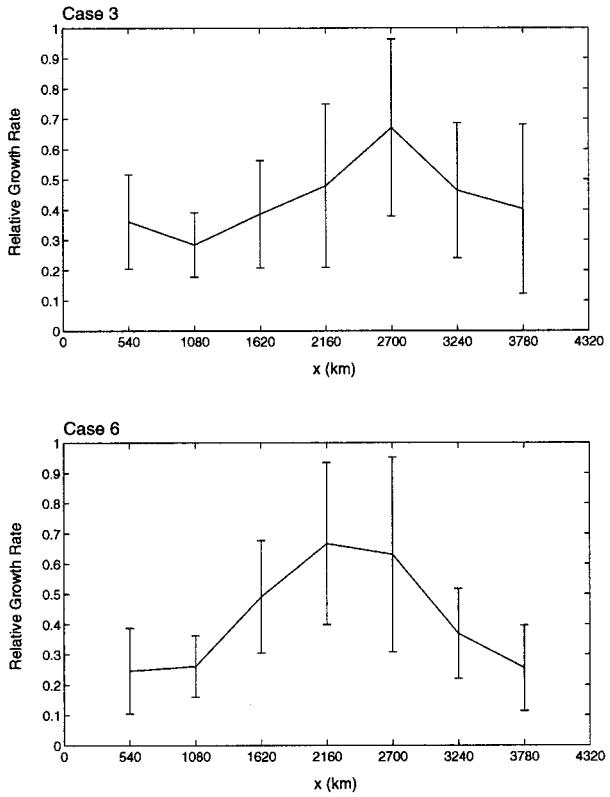

FIG. 6. Relative growth rates computed from instantaneous streamfunction samples from case 3 (top) and case 6 (bottom). See section 5a for a description of the method. The average relative growth rate at each x, defined as the mean of 20 individual samples at each x, is connected by solid lines. One-standard-deviation scatter of the 20 estimates about their average are shown by the vertical bars.

where effects of topography on the flow are weaker and variability in relative growth rates is large. Thus, as with the time mean flow, the meridional topographic slope stabilizes the instantaneous jet in regions upstream and downstream of x_{mid}; these effects of topography do not exert as strong a stabilizing influence near x_{mid} where topographic steering forces the jet into a region of reduced ambient potential vorticity gradient.

b. Implications with regard to eddy parameterization

In addition to offering a possible explanation for the distribution of eddy energy at some locations in the SO, topographic control of flow stability has implications for parameterizing subgrid-scale baroclinic eddies in coarse-resolution ocean models. Because coarse-resolution models do not resolve individual mesoscale eddies, dynamical effects of eddies on the larger-scale flows of interest are parameterized based on properties of the resolved (large scale) flow. Early parameterizations expressed eddy diffusion of heat and momentum in terms of horizontal and vertical gradients of large-scale velocity and temperature (e.g., Bryan and Cox 1968). More recent work modified this formulation to account for the predominance of eddy diffusion along isopycnal surfaces (Solomon 1971; Redi 1982; Gent and McWilliams 1990). Comparisons of the eddy-resolving and non-eddy-resolving simulations demonstrate that isopycnal mixing in the Gent and McWilliams (GM) parameterization provides results superior to the previous Cartesian representations (see Gent et al. 1995; Danabasoglu and McWilliams 1995). Accounting for Richardson-number-dependent spatial variations in the isopycnal diffusion coefficients may further improve coarse-resolution simulations (Visbeck et al. 1997).

For many flow regimes, parameterizing eddy effects in terms of the large-scale flow will provide adequate estimates of heat and momentum fluxes by unresolved baroclinic eddies. However, these parameterizations will not perform as well in regimes where topography controls the production of mesoscale eddies. As shown in section 5a, stabilization of strong baroclinic jets by topographic slopes can lead to concentrations of eddy energy in regions of weak mean shear. The effect of this on the parameterization of eddy fluxes can be evaluated to a limited degree from the two-layer QG model (also see Treguier et al. 1997); because meridional fluxes are of central importance in SO geometry, we will consider only this component. In QG dynamics, the slope of the interface plays the role of the negative of the large-scale temperature gradient (see McWilliams and Chow 1981). Similarly, the eddy flux of thickness at the interface is analogous to the negative of eddy heat flux. As shown in Fig. 7, the largest meridional gradients of interface height in case 6 are located along the jet, far from x_{mid}. In contrast, the time-mean meridional eddy thickness flux is small everywhere, except near x_{mid} where a net northward thickness flux (i.e., a net southward heat flux) is observed (Fig. 7, bottom). Because the strongest gradients of time-mean interface height do not coincide with regions of significant eddy fluxes in this case, eddy fluxes predicted from the large-scale flow, without consideration for the topography, will differ significantly from those computed in the eddy-resolving case.

While deriving an alternative eddy parameterization is beyond the scope of this paper, the results presented here suggest that the contribution of topography to the ambient potential vorticity gradient should be considered in evaluating processes dependent on the spatial distribution of eddy energy; a parameterization in terms of large-scale potential vorticity may produce more realistic coarse-resolution flows. A significant step in this direction has been taken by Treguier et al. (1997). The improvement obtained from including topography in a potential-vorticity-based parameterization will depend on the contribution of topography to the stability of oceanic flows relative to contributions from other processes. In regimes where topography controls flow stability, eddy parameterizations such as GM will not perform well. But, in regimes where variations of topography are weak relative to β, the mechanism described in section 5a is not expected to significantly affect the

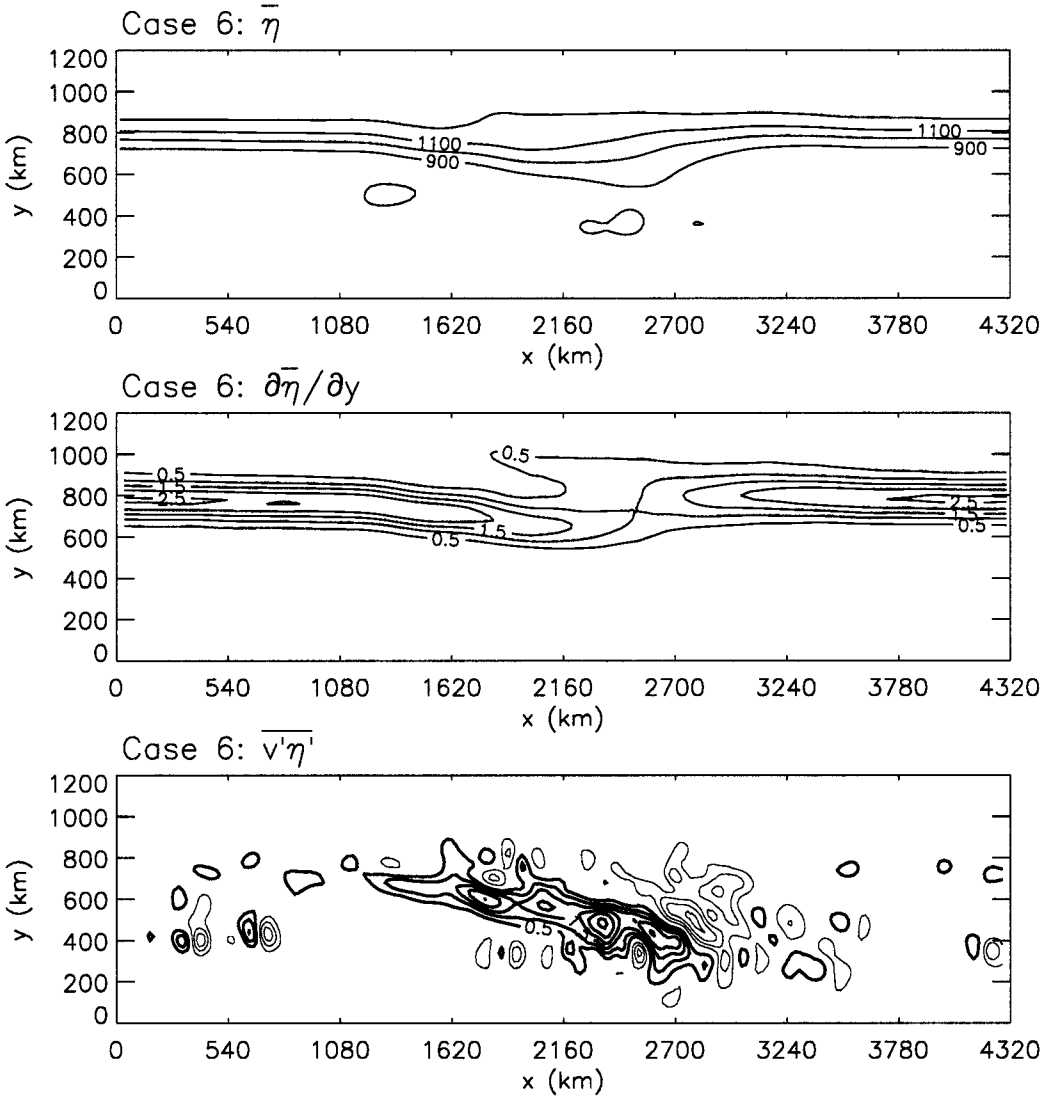

FIG. 7. Time-mean interface height, $\overline{\eta} = H_1 - (f_o/g')(\overline{\psi}_2 - \overline{\psi}_1)$ (top, ci = 100 m), meridional gradient of interface height (center, ci = 0.5 m/km), and meridional eddy thickness flux at the interface (bottom, ci = 0.5 $m^2\ s^{-1}$, positive values in thick contours) for case 6. The zero contour is not plotted in the lower two panels.

spatial distribution of eddy fluxes. Analysis of relations between topography and the large-scale flow from hydrographic data may illuminate the relative importance of this process in the ocean.

6. Energy

The zonal variations of flow stability described above lead to both regional and domain-averaged variations of eddy–mean flow interaction. The sensitivity of eddy–mean flow interaction to zonal modulations of topography are evaluated in this section based on area-averaged, time-mean energy balances (see McWilliams et al. 1978 for a full derivation). Results are displayed as diagrams that follow the key provided in the lower right panel of Fig. 8. In each experiment, the wind is a source of energy for the time-mean field. The time-mean rate of wind energy input depends on the orientation of the time-mean jet, with higher transfer rates occurring for cases with more zonally oriented time-mean flows. Because the wind is steady, eddies receive energy only by conversions from the time-mean flow. Energy is removed from the time-mean flow and from the eddy field by bottom friction and biharmonic lateral friction. The partition of vertical transfers between the time-mean flow and the eddy field depends on the stability of the flow and on feedbacks of eddy energy to the time-mean flow. Note that, while topography does not appear explicitly in the area-averaged energy budgets, the area-averaged energetics can be sensitive to variations of topography if topography induces variations in the flow structure.

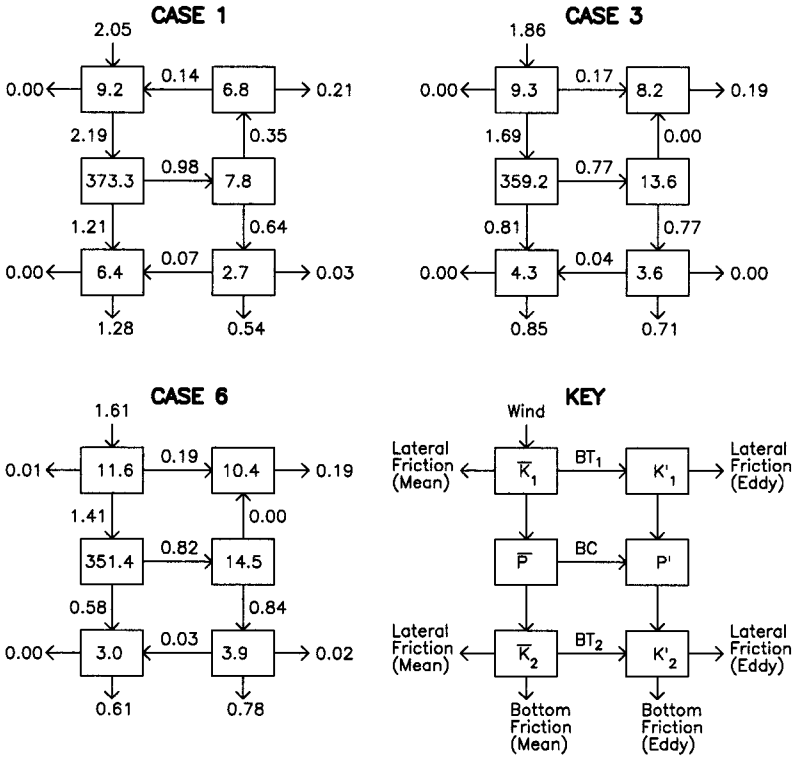

FIG. 8. Area-averaged energy balance diagrams for cases 1, 3, and 6 from the two-layer QG model. Key is shown at the lower right. See McWilliams et al. (1978) for mathematical expressions for each of the energy balance terms.

Comparison of the eddy-mean conversion terms (Fig. 8) shows that there are two dynamically distinct regimes for the cases considered here. In case 1 (and in the flat-bottom case; see McWilliams et al. 1978) the time-mean flow is baroclinically unstable ($\overline{P} \rightarrow P'$). A significant fraction of the energy transferred to the eddy field by flow instabilities is returned to the time-mean flow in the surface layer ($\overline{K}_1 \leftarrow K_1'$). Surface layer eddy kinetic energy is relatively low, and eddies are particularly weak in layer 2. In contrast, in cases 3 and 6, eddies are formed by a mixed baroclinic–barotropic instability process ($\overline{P} \rightarrow P'$ and $\overline{K}_1 \rightarrow K_1'$), and eddy energy is returned to the mean flow only in the deep layer. This allows a more vigorous eddy field in the surface layer and at the interface.

The variations of flow regime inferred from the area-averaged, time-mean energetics can be related to topographically induced variations of time-mean shear. In case 1, the time-mean jet is broad and vertical shear is weak (Fig. 3). Baroclinic conversion rates ($\overline{P} \rightarrow P'$) are, however, comparable to those observed in cases with stronger time-mean baroclinic shear because the quantity of mean potential energy is comparable for the broad, weak jet of case 1 and for the narrower, more baroclinic jets of cases 3 and 6. The shift in dynamics between case 1 versus cases 3 and 6 is primarily related to the breadth of the surface layer jet. In particular, weak shear along the flanks of the jets in case 1 cannot produce a domain-averaged conversion due to barotropic instability ($\overline{K}_1 \rightarrow K_1'$). This conversion is supported by the stronger horizontal shear of the narrower time-mean jets in cases 3 and 6.

As a result of the sensitivity of eddy–mean flow energy conversions to topography, the quantity of eddy energy and the partition of vertical transfers of energy between the time-mean flow and the eddies depend on the topographic configuration. In case 1, 17% of energy transferred to the eddy field by baroclinic instability is returned to the time-mean flow, and vertical energy transfers via the mean flow exceed transfers via the eddies by a more than a factor of 2. Because eddy energy in the lower layer is weak, bottom friction dissipation from the mean flow is the major sink of energy. In contrast, the larger mean-to-eddy energy conversions in cases 3 and 6 produce vigorous baroclinic eddies. Downward energy transfers via the eddies ($P' \rightarrow K_2'$) in these cases are comparable to, or larger than, transfers via the mean flow ($\overline{P} \rightarrow \overline{K}_2$). The deep eddy field is relatively energetic, thus bottom friction dissipation by the eddy field exceeds bottom friction dissipation from the time-mean flow.

7. Vorticity

a. Time-mean vorticity balances

The comparison of energy budgets clearly demonstrates that zonal modulations of topography can fun-

damentally alter flow regimes as well as increase the contribution of the transient component of the flow to time-mean dynamics. To more fully understand the regional importance of transient eddies and the sensitivity of regional dynamics to subtle changes in topography, we consider time-mean vorticity balances. The time-mean QG vorticity budget is derived by decomposing the streamfunction and potential vorticity fields in each layer into time-mean and time-varying components. The resulting balance is given by

$$\frac{\partial}{\partial t}\overline{Q}_n = J(\nabla^2\overline{\psi}_n, \overline{\psi}_n) + J\left(\frac{(-1)^n f_0^2}{g'H_n}(\overline{\psi}_1 - \overline{\psi}_2), \overline{\psi}_n\right) + J(f_0 + \beta y, \overline{\psi}_n)$$
$$+ \overline{J(\nabla^2\psi_n', \psi_n')} + \overline{J\left(\frac{(-1)^n f_0^2}{g'H_n}(\psi_1' - \psi_2'), \psi_n'\right)} + J\left(\frac{f_0 h_b}{H_n}, \overline{\psi}_n\right)\delta_{n,2}$$
$$+ \frac{\text{curl}_z\overline{\boldsymbol{\tau}}}{\rho_0 H_n}\delta_{n,1} - c_b\nabla^2\overline{\psi}_n\delta_{n,2} - A_6\nabla^6\overline{\psi}_n, \tag{3}$$

where symbols and parameters are defined as in Table 1. Because a standard terminology has not been developed for the various terms in Eq. (3), we use the conventions in Table 2 for referring to terms on the right-hand side of Eq. (1). These designations are similar to those used by Holland and Lin (1975) and Holland and Rhines (1980).

Some features of the time-mean vorticity balance are common to all three experiments. In layer 1, wind stress curl (WIND) acts as a source of positive vorticity in the northern half of the domain and negative vorticity in the southern half of the domain. In layer 2, bottom friction (BFRIC) is a sink of vorticity. Contributions to the vorticity budget from lateral friction (LFRIC) are small in both layers owing to the choice of A_6. Other terms in the balance are the result of advection by the time-mean and eddy flow fields. The time-mean and eddy vortex stretching terms (MNST and EDST) transfer vorticity vertically between model layers. The time-mean and eddy relative vorticity terms (MNRV and EDRV) arise from horizontal advection within a model layer. Stretching and shrinking of water columns in regions where the time-mean flow crosses topographic contours transports vorticity within layer 2 (TOPOG); the time-mean meridional velocity transports planetary vorticity within a given model layer (BETA).

Effects of zonal variations of topography on the dynamics of the time-mean flow are inferred from a comparison of individual terms in the time-mean vorticity balance. The time derivative on the left-hand side of Eq. (1) is approximately zero for the statistically steady sampling intervals considered here. This comparison therefore demonstrates effects of each of the nine terms on the rhs of Eq. (1) in maintaining the time-mean distribution of vorticity at each location of the model domain. The value of each term on the rhs of Eq. (1) is displayed for each model layer as a grayscale image for cases 1 and 6 (Figs. 9–12). The x and y axes of each image correspond to the zonal and meridional dimensions of the model domain. Case 3 fields (not shown) are intermediate between the results plotted in Figs. 9–12.

The vorticity balance is relatively simple in case 1. Because the time-mean flow is nearly zonally uniform, terms that depend on the time-mean meridional velocity or on zonal variations of the flow (i.e., BETA, TOPOG, MNST) are small. Although the time-mean relative vorticity advection term (MNRV) can be large locally, decorrelation length scales for this term are short. The contribution to the time-mean vorticity balance from MNRV is therefore negligibly small when averaged over eddy length scales. In layer 1 (Fig. 9), eddy advection of eddy relative vorticity (EDRV) associated with wave formation and eddy detachment along the jet reinforces the input of wind vorticity. The combination of WIND and EDRV is balanced by advection of eddy-stretching vorticity, EDST, which removes positive (negative) vorticity from the surface layer north (south) of the jet axis. Because motions of the interface couple the surface and deep layers, EDST in the surface layer acts as a source of positive (negative) vorticity in the deep layer north (south) of the jet (Fig. 10). Vorticity input to the deep layer by EDST is removed primarily by bottom friction. The balance observed in the flat-bottom case is qualitatively similar; terms in flat-bottom case are, however, symmetric with respect to the zero line of wind stress curl.

Zonal variations of topography dramatically alter regional variations in the time-mean vorticity balance. Terms that are negligibly small in case 1 figure prominently in the balance of case 6. In the surface layer (Fig. 11), these include the time-mean advection terms, MNRV and MNST, and a lesser contribution from advection of planetary vorticity, BETA. In the deep layer (Fig. 12), TOPOG also contributes significantly. These

TABLE 2. Time-mean vorticity balance terms.

MNRV	$J(\nabla^2\overline{\psi}_n, \overline{\psi}_n)$	mean advection of mean relative vorticity
MNST	$J\left(\frac{(-1)^n f_0^2}{g' H_n}(\overline{\psi}_1 - \overline{\psi}_2), \overline{\psi}_n\right)$	mean advection of mean stretching vorticity
BETA	$J(f_0 + \beta y, \overline{\psi}_n)$	mean advection of planetary vorticity
EDRV	$\overline{J(\nabla^2\psi_n', \psi_n')}$	time-mean of the eddy advection of eddy relative vorticity
EDST	$\overline{J\left(\frac{(-1)^n f_0^2}{g' H_n}(\psi_1' - \psi_2'), \psi_n'\right)}$	time-mean of the eddy advection of eddy-stretching vorticity
TOPOG	$J(f_0 h_b/H_n, \overline{\psi}_n)\delta_{n,2}$	mean advection of topographic vorticity
WIND	$\mathrm{curl}_z\frac{\overline{\boldsymbol{\tau}}}{\rho_0 H_n}\delta_{n,1}$	wind vorticity
BFRIC	$-c_b\nabla^2\overline{\psi}_n\delta_{n,2}$	bottom friction vorticity
LFRIC	$-A_6\nabla^6\overline{\psi}_n$	lateral friction vorticity

additional contributions arise due to (1) alongstream variations of the horizontal and vertical shear of the time-mean jet and (2) meridional deflections of the time-mean jet.

Regional variations of vorticity can be divided into regimes pertaining to values of x near x_{mid} and values of x far upstream or far downstream of x_{mid}. Upstream of x_{mid} and in the far downstream region, time-dependent eddies associated with meandering of the core of the jet contribute to a local balance of time-mean vorticity, similar to that observed in case 1. In these regions of nearly zonal time-mean flow, the primary balance in the surface layer is among WIND, EDRV, and EDST; the primary balance in the deep layer is between EDST and BFRIC. Near x_{mid}, a very different local balance of time-mean vorticity is observed. Unlike case 1, along-channel variations of layer 1 time-mean shear (MNRV) contribute significantly to the balance. In addition, the BETA

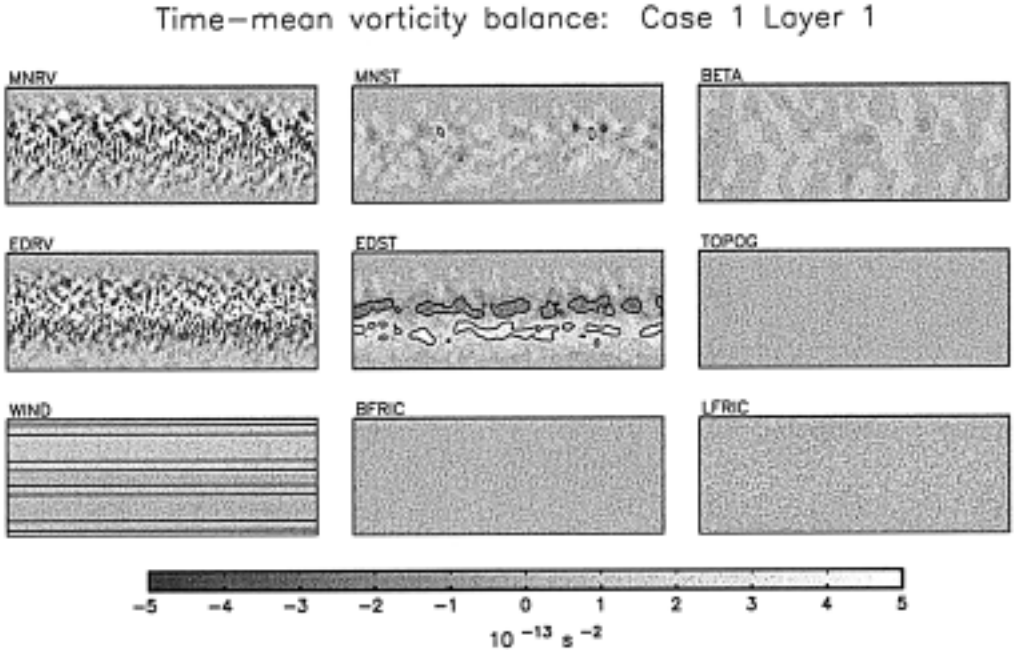

FIG. 9. Layer 1 vorticity balance terms for case 1 (plan view). See Table 2 for definitions. The contour interval is 2.5×10^{-14} s^{-2} for WIND, 1.0×10^{-12} s^{-2} for MNRV and EDRV, and 2.5×10^{-13} s^{-2} for all other terms; TOPOG and BFRIC are zero in this layer. The zero contour is omitted.

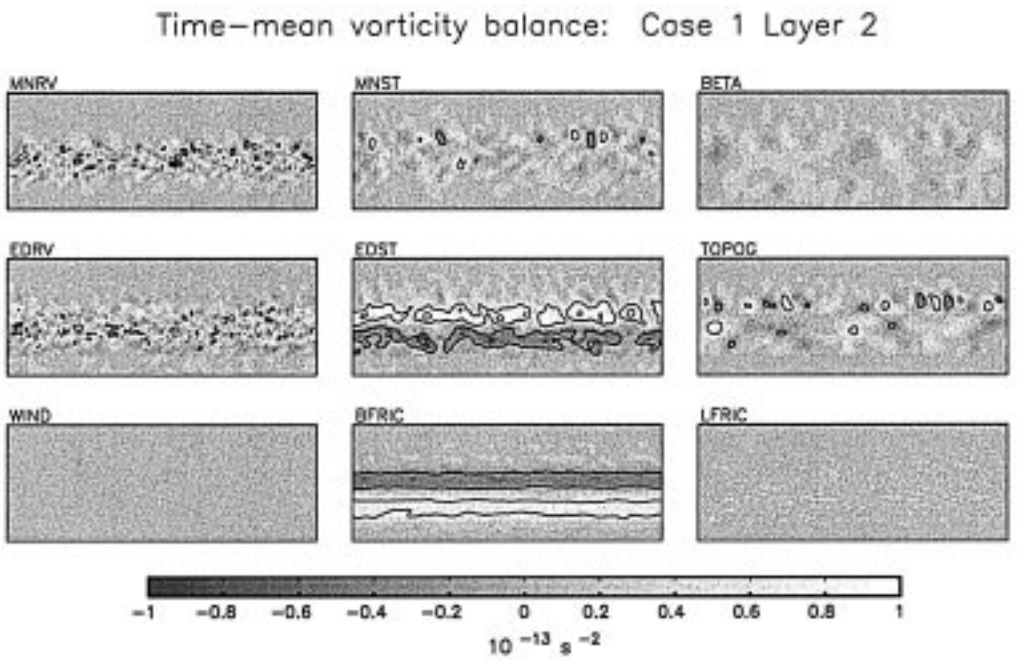

FIG. 10. Layer 2 vorticity balance terms for case 1 (plan view). See Table 2 for definitions. The contour interval is 5.0×10^{-14} s^{-2} for all terms; WIND is zero is this layer. The zero contour is omitted.

and MNST terms are nonzero in layer 1 near x_{mid} due to meridional deflections of the time-mean jet. Eddy advection of eddy relative vorticity (EDRV) and eddy advection of eddy-stretching vorticity (EDST) are both locally intensified near the local maximum of K_1' downstream of x_{mid}.

The zonal modulations of the stretching terms in the layer 1 balance near x_{mid} have particularly important

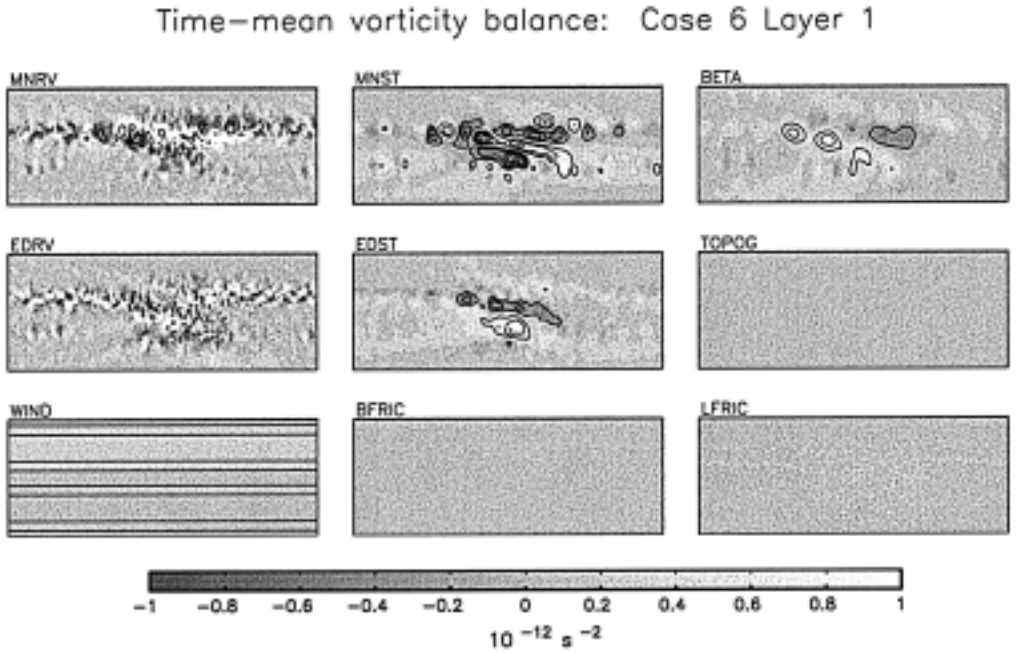

FIG. 11. Layer 1 vorticity balance terms for case 6 (plan view). See Table 2 for definitions. The contour interval is 2.5×10^{-14} s^{-2} for WIND, 2.0×10^{-12} s^{-2} for MNRV and EDRV, and 5.0×10^{-13} s^{-2} for all other terms; TOPOG and BFRIC are zero in this layer. The zero contour is omitted.

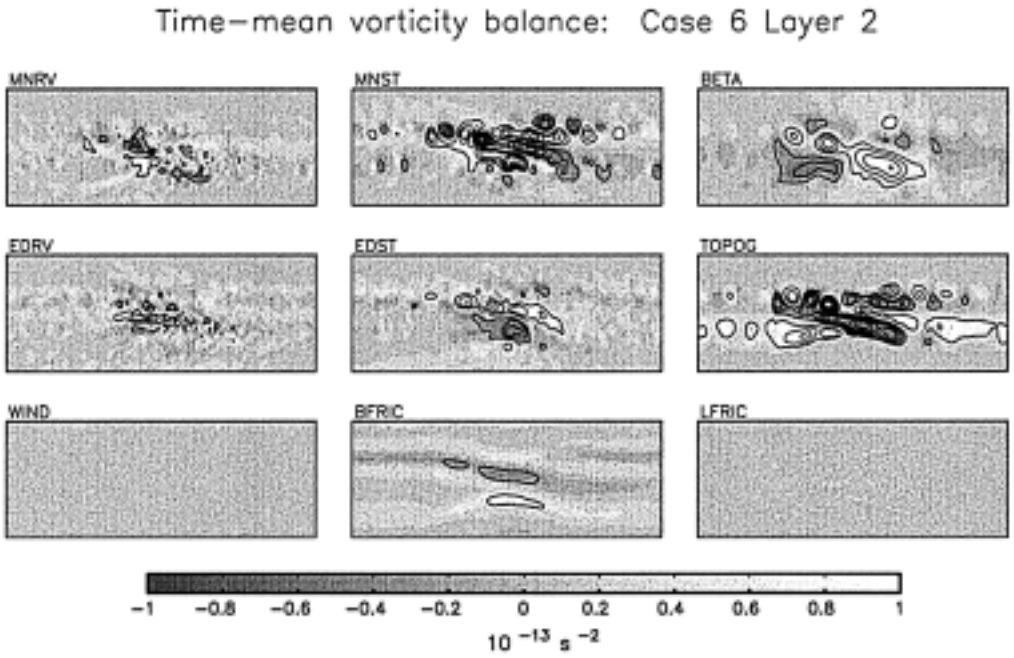

FIG. 12. Layer 2 vorticity balance terms for case 6 (plan view). See Table 2 for definitions. The contour interval is 5.0×10^{-14} s^{-2} for all terms; WIND is zero in this layer. The zero contour is omitted.

consequences for the layer 2 balance. Because these terms are the only means available for transferring vorticity from the surface to the deep layer, the zonal modulation of topography localizes the input of vorticity to layer 2. This localization can be compared with the balance observed in case 1, where vorticity is added to layer 2 nearly uniformly along the jet. While the relative vorticity advection terms (MNRV and EDRV) in case 6 could potentially redistribute vorticity beyond x_{mid} by horizontal advection, these terms are small in layer 2 due to the weak time-mean meridional velocities and to the generally low levels of eddy energy far upstream and downstream of x_{mid}. As a result of the small mean meridional velocities over much of the channel, BETA and TOPOG do not contribute significantly to the time-mean vorticity budget in regions distant from the modulation of topography. Vorticity added to layer 2 near x_{mid} is therefore removed locally by bottom friction. BFRIC is largest at the narrowest segment of the ridge where time-mean horizontal shear is largest. Thus, the distinguishing property of the vorticity balance for the cases 3 and 6 cases is that zonal modulations of topography locally intensify the export of vorticity from layer 1 and the input of vorticity to layer 2, producing regional variations in the vorticity distribution and in the vorticity dynamics.

b. Eddy contribution to the balance of time-mean vorticity

The effect of eddies in maintaining the local distribution of time-mean vorticity can be evaluated from the sum of the eddy flux of eddy relative vorticity and the eddy flux of eddy stretching vorticity. This sum is plotted in Fig. 13 for the surface layer for cases 1, 3, and 6. In layer 2, the net effect of the eddies is approximately equal to EDST owing to the weak contribution from EDRV.

It is important to note that eddies are a fundamental part of the model dynamics for all of the cases considered here. Even in the case with zonally uniform topography, eddies are an important conduit for vertical transfers of vorticity (Figs. 9–10), and the development of a vigorous eddy field is required to attain a statistically steady solution. However, for the zonally uniform topography, the net effect of eddies on the time-mean balance of vorticity in the surface layer is quantitatively small owing to a near cancellation between the EDRV and EDST terms. Eddies emerge as a more important net contribution to the balance when a local accumulation of eddy energy is supported by a localized forcing mechanism.

Not surprisingly, the net eddy contribution to the time-mean vorticity balance is largest in regions of high eddy energy (Fig. 13). In cases 3 and 6, eddies are a net negative contribution to the vorticity balance along the south flank of the time-mean jet near x_{mid}. Along the north flank of the time-mean jet near x_{mid} eddies are a net positive contribution to the vorticity balance. These contributions can be compared with the sign of the wind contribution to the time-mean vorticity balance (i.e., negative in the southern half of the domain, positive in the northern half of the domain), demonstrating

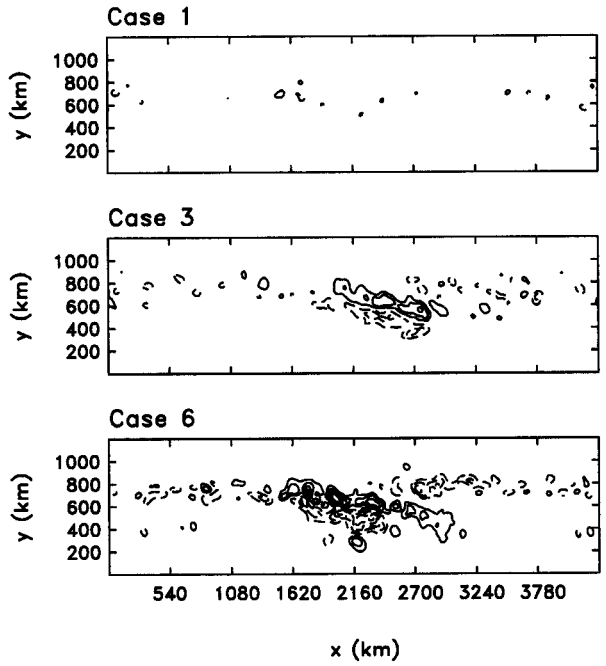

FIG. 13. The total eddy contribution to the time-mean vorticity balance for cases 1, 3, and 6 (ci = 5.0×10^{-13} s^{-2}). Solid contours correspond to positive values. Dashed contours correspond to negative values. The zero contour is omitted.

that eddies reinforce the input of wind vorticity in the region near the zonal modulation of topography. Farther downstream, the net eddy contribution opposes the input of vorticity by the wind.

The systematic contribution of eddies to the local vorticity balance, and the magnitude of the net eddy contribution relative to other terms in the balance, suggests that accurate assessments of the dynamics of time-mean oceanic flows and accurate simulations of time-mean model flows must account for effects of the eddy field on the time-mean dynamics. While this task is presently beyond the capability of many observational systems, it can be accomplished in models by either explicitly resolving mesoscale eddies or by accounting for effects of topography on eddy development with appropriate parameterizations.

c. Alongstream averaged vorticity balances

As noted above, contributions to local vorticity balances are approximately oriented along time-mean streamlines. The effects of local variations of topography on large-scale vorticity dynamics can therefore be gauged by averaging each contribution to the time-mean vorticity balance along time-mean streamlines (Fig. 14). This averaging procedure is preferred over other methods (e.g., a zonal average) because streamwise coordinates reflect the geometry of the problem with greater fidelity. The alongstream averaged balances for cases 1 and 6 can be compared with the local vorticity analyses presented in Figs. 9–12. The alongstream averaged balances are also shown for case 3 to better illustrate the progression of vorticity changes induced by the zonal modulation of topography.

In the surface layer (Fig. 14), the primary effect of zonal variations of topography is to retain a larger number of terms in the balance. In case 1, a vigorous eddy field is required to satisfy the large-scale balance of vorticity. Eddies redistribute vorticity input to the surface layer by the wind and transfer it downward to layer 2 where it is dissipated by bottom friction. Terms dependent on meridional deflections of the jet (e.g., MNST and BETA) and on zonal variations of mean shear (e.g., MNRV) are zero in case 1 owing to the strictly zonal nature of the mean flow and the topography; these terms contribute significantly to the surface layer balance for cases 3 and 6. It is clear from Fig. 14 that magnitudes of the alongstream averaged contributions from the individual eddy terms are reduced as the zonal modulation of topography is introduced. However, the net contribution from the eddy terms increases with increasing zonal modulations of the topography (also see Fig. 13). Thus, while eddies are important to the time-mean dynamics for all of the cases considered here, transient eddies are particularly important to both the local and large-scale dynamics for cases with large alongstream variations of topography.

In layer 2 (see Fig. 15), zonal variations of topography affect the relative contributions of all terms to the balance. In cases 1 and 3, the input of vorticity to layer 2 by EDST is balanced primarily by bottom friction. The overall balance of time-mean vorticity is, however, very different in these two cases owing to the contribution of TOPOG. TOPOG is zero in case 1 where the time-mean jet follows topographic contours. In contrast, it is one of the larger contributions in case 3, in which the time-mean jet crosses isobaths near x_{mid}. Alongstream variations of mean shear and interface height, which occur as a result of topographic steering in cases 3 and 6, produce moderate contributions from BETA, MNST, and MNRV, which approximately balances the contribution from TOPOG. In comparison with cases 1 and 3, flow in the time-mean deep jet is sluggish in case 6 (see Fig. 3) leading to the relatively minor contribution of bottom friction. The topographic term is therefore balanced by steering of the time-mean jet (BETA) and by eddy stretching (EDST) associated with vorticity fluxes from the baroclinic eddies.

8. Discussion

Geographic variability of the dynamics of the ACC have only recently begun to be addressed from in situ observations of ACC dynamics. According to one long-standing theory of SO dynamics (Munk and Palmén 1951), the input of eastward momentum by the wind in the circumpolar region is balanced by the loss of momentum via topographic form stress. Because there are

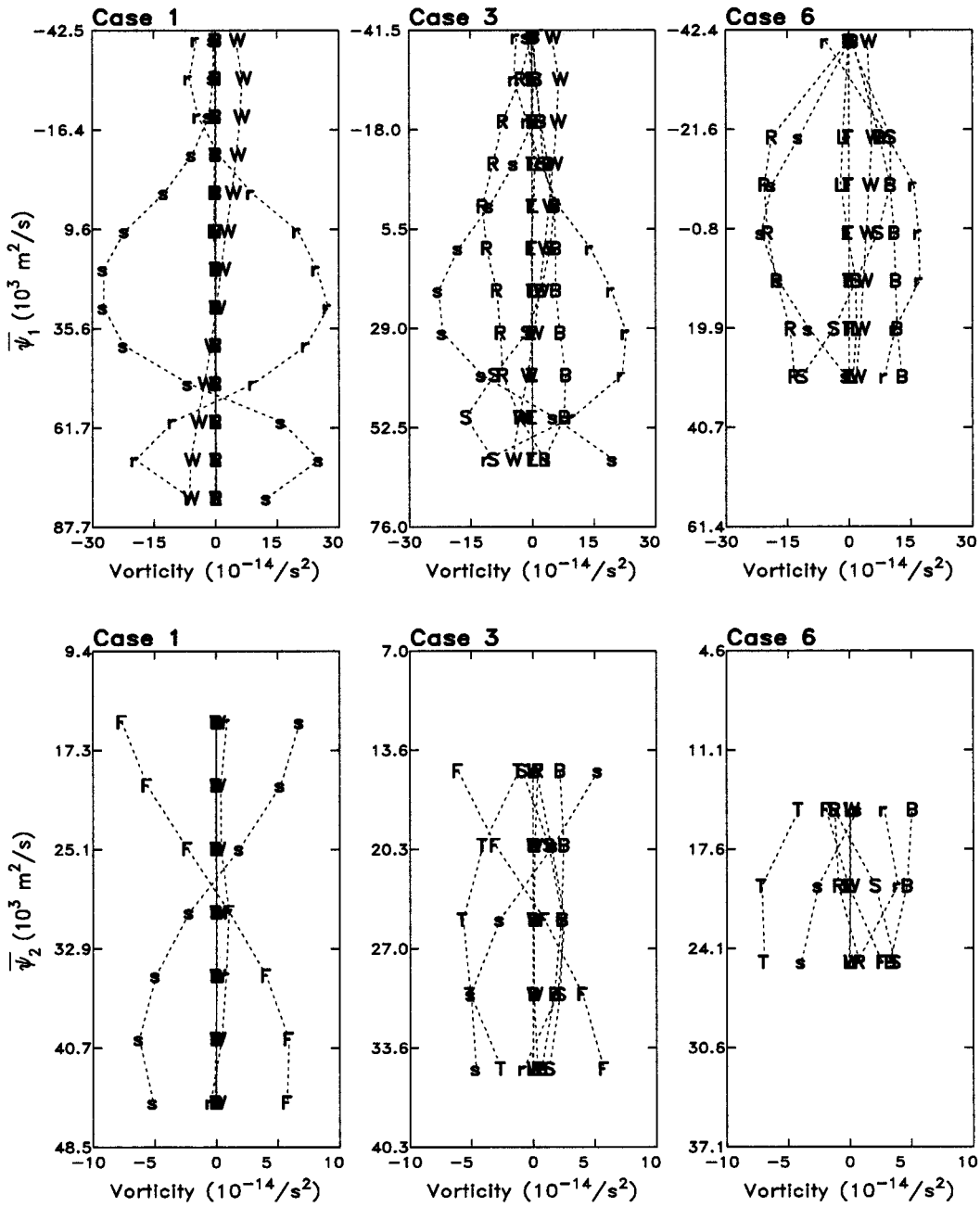

FIG. 14. Contributions to the time-mean vorticity balance averaged along time-mean streamlines for layer 1 (top row) and layer 2 (bottom row). Terms in the vorticity balance include MNRV (R), MNST (S), BETA (B), EDRV (r), EDST (s), TOPOG (T), WIND (W), BFRIC (F), and LFRIC (L) (see Table 2). Note that streamfunction values increase to the south (see Fig. 2). For each case, balances are averaged only for streamlines that have a single position y for each along-channel location x (i.e., streamlines comprising the time-mean jet, not those near the channel walls).

few locations where topography breaches the surface along the path of the ACC, this balance requires a vertical transfer of momentum from the surface to the depth of topographic obstacles. One mechanism that has been proposed for this transfer is a downward flux of momentum by transient eddies (Johnson and Bryden 1989). Such fluxes may arise in conjunction with southward heat transport by baroclinic instability.

This conceptual model was tested by Johnson and Bryden (1989) who calculated the downward momentum flux from baroclinic eddies in Drake Passage. Eddy heat fluxes were estimated from observations at the ISOS central Drake Passage current meter array. Properties of the large-scale flow were measured from a hydrographic section across Drake Passage. From these data, Johnson and Bryden found that Drake Passage

eddies transport approximately twice as much momentum downward through the water column as is supplied locally by the wind. To account for this local imbalance, Johnson and Bryden suggested that horizontal eddy momentum fluxes may locally intensify the flow in Drake Passage, thereby increasing downward momentum flux at the central Drake Passage current meter array. Alternatively, they hypothesized that eddy fluxes need not balance the wind locally.

In this paper, we have evaluated local dynamics from vorticity balances (§7) rather than momentum balances. This strategy is used because unknown ageostrophic contributions to the momentum equations for the QG model used here do not allow a full reconstruction of the momentum balance at each point in the model domain.[2] The vorticity analyses presented in section 7 demonstrate that alongstream variations of topography can shift the region of eddy-influenced dynamics within the model domain. In an experiment with zonally uniform topography (e.g., case 1), the production of time-dependent eddies, the transfer of vorticity to the deep layer, and the dissipation of vorticity by bottom friction occur along the entire jet. In cases with a zonal modulation of topography, the largest terms in the time-mean vorticity balance, including contributions from transient eddies, are locally intensified near the alongstream variation of topography.

Because alongstream variations of topography redistribute eddy fluxes, the input of vorticity by the wind is not locally balanced by export of vorticity to layer 2 in the cases described here. Instead, wind vorticity is broadly distributed over the model domain and downward transfers of vorticity by eddy stretching are confined to regions where the zonal variation of topography allows enhanced eddy development. Because vertical transfers of vorticity and momentum both require interfacial stretching, downward fluxes of momentum may be large in the same regions. Results of this idealized study therefore support one of the hypotheses put forth by Johnson and Bryden (1989), namely that the dynamics of the SO do not represent a local balance. Areas where topography destabilizes the time-mean flow may be regions of locally enhanced vertical fluxes of vorticity and momentum in the ACC. These regions may also be particularly important sinks of vorticity and sites of enhanced energy dissipation.

9. Conclusions

In this study, we have considered effects of zonal variations of zonal ridge topography on the structure and stability of the time-mean flow and on the distribution and dynamical contributions of time-dependent eddies. The model topography (Fig. 2) consists of a zonal ridge with a zonal modulation of ridge height (case 3) or ridge height and width (case 6). The case 6 topography is intended as an idealized representation of the Southeast Indian Ridge near the Australian–Antarctic Discordance (see Fig. 1). In the region near the AAD, locally high values of sea level variability are found downstream of the point of minimum ridge height and width; variability decreases farther downstream and to the north and south of the ridge.

While the simple dynamics and geometry used here cannot produce the full range of complexity observed in the ocean, it is encouraging that the model captures basic features of the altimeter and in situ observations. For a ridge with a zonal modulation in height and width, the surface-layer eddy kinetic energy distribution in the model is qualitatively similar to the distribution of sea level variability near the AAD from Geosat (Figs. 1 and 4). In addition, the structure of the layer 1 time-mean flow in the model is in good qualitative agreement with the structure of the ACC determined from hydrographic data (Callahan 1971; Savchenko et al. 1978; Gordon et al. 1978) and with the axis of the ACC estimated from altimeter observations (Morrow et al. 1994).

Based on results from these numerical simulations, effects of topography on flow stability may explain the correlation between eddy variability and topography in some regions of the SO. Analysis of flow fields and dynamics from the two-layer QG model indicate that alongstream variations of topography produce local variations of flow stability through the combined action of topographic steering and the effect of topographic slopes on the ambient potential vorticity gradient. Variations of topography that steer the jet into regions of reduced ambient potential vorticity gradient coincide with local minima of flow stability; eddy energy is concentrated downstream of these locations. Jet flow in regions where topographic slopes increase the ambient potential vorticity gradient is more stable, and the overlying eddy field is less energetic.

One interesting consequence of the zonal variation of flow stability is that, even in segments of the channel where the topography is zonally uniform (e.g., $x < 1620$ km and $x > 3240$ km), the structure of the time-mean flow differs significantly for cases with and without a zonal modulation of topography. The most dramatic evidence of this is the difference in width of the surface-layer jet for cases 1 and 6 (Fig. 3). In case 1, topographic steering does not stabilize the jet as effectively as in case 6. As a result, instabilities are produced at relatively low values of vertical and horizontal shear. As these instabilities grow and detach from the jet as closed rings, their kinematic effect is to broaden the meridional profile of the time-mean jet. In contrast, topographic steering in case 6 stabilizes the flow in the region far from x_{mid}. Waves propagating along the jet in this area are stable and of small amplitude. The time-mean flow is

[2] Other papers using QG dynamics in channel domains, e.g., McWilliams et al. (1978) and Treguier and McWilliams (1990), have circumvented this difficulty by zonal averaging in cases where the statistics of the topography are zonally homogeneous.

therefore less affected by the meridional mixing of momentum associated with eddies, and a narrower jet core is evident in the time-mean streamlines. The difficulty of separating the time-mean and eddy fields is a long-standing challenge for studies of eddy–mean flow interaction. It is encouraging that qualitatively similar conclusions are obtained from linear stability analysis of either the time-mean jet or of instantaneous velocity profiles.

Topographic control of flow stability represents a mechanism that is not considered in commonly used eddy parameterizations for coarse-resolution primitive-equation ocean models (e.g., Gent and McWilliams 1990). Results from this paper suggest that an eddy parameterization based on vorticity, rather than shear, may produce more realistic large-scale flows. Recent work by Treguier et al. (1997) is a significant step in this direction. The benefit of accounting for effects of topography on flow stability in eddy parameterizations will depend on the degree to which oceanic flows are affected by the mechanism described here. This sensitivity has not been quantified in this paper for realistic oceanic regimes; such assessments would require a more sophisticated model or a careful analysis of in situ data.

A second important conclusion from the experiments discussed here is that alongstream modulations of topography alter area-averaged, alongstream averaged, and local dynamical balances by modifying the structure of the large-scale flow and shifting the region of eddy-influenced dynamics to areas near alongstream topographic gradients. While transient eddies are an active component of the time-mean, area-averaged dynamics for both zonally uniform and zonally variable topographies, weak zonal modulations of topography can fundamentally alter the area-averaged dynamical regime. Flow over zonally uniform topography is baroclinically unstable in the simulations considered here. The introduction of a zonal modulation of topography results in a regime of mixed baroclinic–barotropic instability. The difference between these two regimes can be traced to the sensitivity of time-mean horizontal shear to alongstream variations of topography.

In addition to effects of topographic variations on area-averaged dynamics, significant local effects of topography are observed. The redistribution of vorticity fluxes associated with zonal modulations of topography are particularly dramatic (see Figs. 9–12). This redistribution affects the mean-flow terms as well as eddy–mean flow interaction terms in the time-mean vorticity balance. In cases with zonal modulations of topography, the input of vorticity by the wind is not locally balanced by the export of vorticity to layer 2. Instead, wind vorticity is input over a broad region of the model domain; vertical transfers of vorticity by eddy stretching are confined to regions near zonal modulations of topography. Because vertical transfers of vorticity and momentum both require interfacial stretching, downward fluxes of momentum may be large in the same regions. Furthermore, the greater role of eddy energy dissipation for cases with zonal modulations of topography (Fig. 8) suggests that these regions may also be sites of particularly strong energy dissipation by bottom friction. Results from these simulations therefore support the hypothesis of Johnson and Bryden (1989), who suggested that momentum added to the SO by the wind is not removed locally.

The sensitivity of area-averaged and local dynamical balances to relatively weak zonal modulations of topography has implications for efforts aimed at modeling SO circulation using near-eddy-resolving primitive equation models. While eddy variability in the present generation of primitive-equation circumpolar ocean models is in good qualitative agreement with observations near large-scale topographic features, these models often fail to produce observed patterns of eddy variability near intermediate-scale topography (see Semtner 1995; Gille 1995). The simulations considered here highlight the potential importance of intermediate-scale topographic features to local and large-scale dynamics, as well as the dynamical importance of horizontal shear associated with oceanic jet flows. Results from this study suggest that improved representations of SO dynamics might be obtained from the present generation of primitive equation models if dynamical effects of topography are modeled with greater fidelity. Resolving horizontal shear across ACC jets, and modeling effects of topographic slope on jet stability, may be of key importance.

Acknowledgments. We thank James Richman, John Allen, Michael Freilich, and Ricardo Matano for their helpful comments throughout this project. We also thank two anonymous reviewers for their constructive comments on the manuscript. The research described here was supported by Grant NAGW-3510 from the National Aeronautics and Space Administration and by Contract 958127 from the Jet Propulsion Laboratory funded under the TOPEX Announcement of Opportunity.

REFERENCES

Belkin, I. M., and A. L. Gordon, 1996: Southern Ocean fronts from the Greenwich meridian to Tasmania. *J. Geophys. Res.,* **101,** 3675–3696.

Bryan, K., and M. D. Cox, 1968: A nonlinear model of an ocean driven by wind and differential heating. Part I: Description of the three-dimensional velocity and density fields. *J. Atmos. Sci.,* **25,** 945–967.

Bryden, H. L., 1979: Poleward heat flux and conversion of available potential energy in Drake Passage. *J. Mar. Res.,* **37,** 1–22.

——, 1983: The Southern Ocean. *Eddies in Marine Science,* A. R. Robinson, Ed., Springer-Verlag, 265–277.

——, and R. A. Heath, 1985: Energetic eddies at the northern edge of the Antarctic Circumpolar Current in the Southwest Pacific. *Progress in Oceanography,* Vol. 14, Pergamon, 65–87.

Callahan, J. E., 1971: Velocity structure and flux of the Antarctic Circumpolar Current south of Australia. *J. Geophys. Res.,* **76,** 5859–5864.

Chelton, D. B., M. G. Schlax, D. L. Witter, and J. G. Richman, 1990: Geosat altimeter observations of the surface circulation of the Southern Ocean. *J. Geophys. Res.,* **95,** 17 877–17 903.

Danabasoglu, G., and J. C. McWilliams, 1995: Sensitivity of the global ocean circulation to parameterizations of mesoscale tracer transports. *J. Climate*, **8,** 2967–2987.

deSzoeke, R. A., and M. D. Levine, 1981: The advective flux of heat by mean geostrophic motions in the Southern Ocean. *Deep-Sea Res.*, **28A,** 1057–1085.

Gent, P. R., and J. C. McWilliams, 1990: Isopycnal mixing in ocean circulation models. *J. Phys. Oceanogr.*, **20,** 150–155.

——, J. Willebrand, T. J. McDougall, and J. C. McWilliams, 1995: Parameterizing eddy-induced tracer transports in ocean circulation models. *J. Phys. Oceanogr.*, **25,** 463–474.

Gill, A. E., 1968: A linear model of the Antarctic circumpolar current. *J. Fluid Mech.*, **32,** 465–488.

——, and K. Bryan, 1971: Effects of geometry on the circulation of a three-dimensional southern-hemisphere ocean model. *Deep-Sea Res.*, **18,** 685–721.

Gille, S. T., 1995: Dynamics of the Antarctic Circumpolar Current: Evidence for topographic effects from altimeter data and numerical model output. Ph.D. thesis, Massachusetts Institute of Technology and Woods Hole Oceanographic Institution, 217 pp.

——, 1997a: Why potential vorticity is not conserved along mean streamlines in a numerical Southern Ocean. *J. Phys. Oceanogr.*, **27,** 1286–1299.

——, 1997b: The Southern Ocean momentum balance: evidence for topographic effects from numerical model output and altimeter data. *J. Phys. Oceanogr.*, **27,** 2219–2232.

Gordon, A. L., E. Molinelli, and T. Baker, 1978: Large-scale relative dynamic topography of the Southern Ocean. *J. Geophys. Res.*, **83,** 3023–3032.

Haidvogel, D. B., and W. R. Holland, 1978: The stability of ocean currents in eddy-resolving general circulation models. *J. Phys. Oceanogr.*, **8,** 393–413.

Hayes, D. E., and J. R. Conolly, 1972: Morphology of the Southeast Indian Ocean. Antarctic Oceanology II: The Australian-New Zealand Sector. *Anta. Res. Ser.*, **19,** 125–145.

Holland, W. R., 1978: The role of mesoscale eddies in the general circulation of the ocean—Numerical experiments using a wind-driven quasi-geostrophic model. *J. Phys. Oceanogr.*, **8,** 363–391.

——, and L. B. Lin, 1975: On the generation of mesoscale eddies and their contribution to the oceanic general circulation. I. A preliminary numerical experiment. *J. Phys. Oceanogr.*, **5,** 642–657.

——, and D. B. Haidvogel, 1980: A parameter study of the mixed instability of idealized ocean currents. *Dyn. Atmos. Oceans*, **4,** 185–215.

——, and P. B. Rhines, 1980: An example of eddy-induced ocean circulation. *J. Phys. Oceanogr.*, **10,** 1010–1031.

Hughes, C. W., and P. D. Killworth, 1995: Effects of bottom topography in the large-scale circulation of the Southern Ocean. *J. Phys. Oceanogr.*, **25,** 2485–2497.

Inoue, M., 1985: Modal decomposition of the low-frequency currents and baroclinic instability at Drake Passage. *J. Phys. Oceanogr.*, **15,** 1157–1181.

Ivchenko, V. O., K. J. Richards, and D. P. Stevens, 1996: The dynamics of the Antarctic Circumpolar Current. *J. Phys. Oceanogr.*, **26,** 753–774.

Johnson, G. C., and H. L. Bryden, 1989: On the size of the Antarctic Circumpolar Current. *Deep-Sea Res.*, **36,** 39–53.

Johnson, J. A., and R. B. Hill, 1975: A three-dimensional model of the Southern Ocean with bottom topography. *Deep-Sea Res.*, **22,** 745–751.

Killworth, P. D., and M. M. Nanneh, 1994: Isopycnal momentum budget of the Antarctic Circumpolar Current in the Fine Resolution Antarctic Model. *J. Phys. Oceanogr.*, **24,** 1201–1223.

Marshall, D., 1995a: Influence of topography on the large-scale ocean circulation. *J. Phys. Oceanogr.*, **25,** 1622–1635.

——, 1995b: Topographic steering of the Antarctic Circumpolar Current. *J. Phys. Oceanogr.*, **25,** 1636–1650.

McCartney, M. S., 1976: The interaction of zonal currents with topography with applications to the Southern Ocean. *Deep-Sea Res.*, **23,** 413–427.

McWilliams, J. C., 1977: A note on a consistent quasigeostrophic model in a multiply connected domain. *Dyn. Atmos. Oceans*, **1,** 427–441.

——, and J. H. S. Chow, 1981: Equilibrium geostrophic turbulence I: A reference solution in a β-plane channel. *J. Phys. Oceanogr.*, **11,** 921–949.

——, W. R. Holland, and J. H. S. Chow, 1978: A description of numerical Antarctic Circumpolar Currents. *Dyn. Atmos. Oceans*, **2,** 213–291.

Morrow, R., R. Coleman, J. Church, and D. Chelton, 1994: Surface eddy momentum flux and velocity variances in the Southern Ocean from Geosat altimetry. *J. Phys. Oceanogr.*, **24,** 2050–2071.

Munk, W. H., and E. Palmén, 1951: Note on the dynamics of the Antarctic Circumpolar Current. *Tellus*, **3,** 53–55.

Orlanski, I., 1969: The influence of bottom topography on the stability of jets in a baroclinic fluid. *J. Atmos. Sci.*, **26,** 1216–1232.

Patterson, S. L., 1985: Surface circulation and kinetic energy distributions in the Southern Hemisphere oceans from FGGE drifting buoys. *J. Phys. Oceanogr.*, **15,** 865–884.

Pedlosky, J., 1987: *Geophysical Fluid Dynamics.* Springer-Verlag, 710 pp.

Peterson, R. G., W. D. Nowlin, and T. Whitworth, 1982: Generation and evolution of a cyclonic ring at Drake Passage in early 1979. *J. Geophys. Res.*, **92,** 712–719.

Pierrehumbert, R. T., 1986: The effect of local baroclinic instability on zonal inhomogeneities of vorticity and temperature. *Advances in Geophysics*, Vol. 29, Academic Press, 165–182.

Redi, M. H., 1982: Oceanic isopycnal mixing by coordinate rotation. *J. Phys. Oceanogr.*, **12,** 1154–1158.

Samelson, R. M., and J. Pedlosky, 1990: Local baroclinic instability of flow over variable topography. *J. Fluid Mech.*, **221,** 411–436.

Sandwell, D. T., and B. H. Zhang, 1989: Global mesoscale variability from Geosat Exact Repeat Mission: Correlation with ocean depth. *J. Geophys. Res.*, **94,** 17 971–17 984.

Savchenko, V. G., W. J. Emery, and O. A. Vladimirov, 1978: A cyclonic eddy in the Antarctic Circumpolar Current south of Australia: results of Soviet-American observations aboard the R/V *Professor Zubov*. *J. Phys. Oceanogr.*, **8,** 825–837.

Semtner, A. J., 1995: Modeling ocean circulation. *Science*, **269,** 1379–1385.

——, and R. M. Chervin, 1988: A simulation of the global ocean circulation with resolved eddies. *J. Geophys. Res.*, **93,** 15 502–15 522.

——, and ——, 1992: Oceanic general circulations from a global eddy-resolving model. *J. Geophys. Res.*, **97,** 5493–5550.

Solomon, H., 1971: On the representation of isentropic mixing in ocean circulation models. *J. Phys. Oceanogr.*, **1,** 233–234.

Treguier, A. M., and J. C. McWilliams, 1990: Topographic influences on wind-driven, stratified flow in a β-plane channel: An idealized model for the Antarctic Circumpolar Current. *J. Phys. Oceanogr.*, **20,** 321–343.

——, I. M. Held, and V. D. Larichev, 1997: Parameterization of quasigeostrophic eddies in primitive equation ocean models. *J. Phys. Oceanogr.*, **27,** 567–580.

Visbeck, M., J. Marshall, T. Haine, and M. Spall, 1997: On the specification of eddy transfer coefficients in coarse-resolution ocean circulation models. *J. Phys. Oceanogr.*, **27,** 381–402.

Webb, D. J., P. D. Killworth, A. C. Coward, and S. R. Thompson, 1991: *The FRAM Atlas of the Southern Ocean.* Natural Environment Research Council, 67 pp.

Wells, N. C., and B. A. deCuevas, 1995: Depth integrated vorticity budget of the Southern Ocean from a general circulation model. *J. Phys. Oceanogr.*, **25,** 2569–2582.

Witter, D. L., 1995: Unstable jet flow along zonal ridge topography. Ph.D. thesis, Oregon State University, 183 pp.

Wolff, J.-O., E. Maier-Reimer, and D. J. Olbers, 1991: Wind driven flow over topography in a zonal β-plane channel: A quasigeostrophic model of the Antarctic Circumpolar Current. *J. Phys. Oceanogr.*, **21,** 236–264.